



HAL
open science

Strain localization in the Alloy 718 Ni-based superalloy: From room temperature to 650 °C

Damien Texier, Julien Milanese, Malo Jullien, Julien Genee, Jean-Charles Passieux, Didier Bardel, Eric Andrieu, Marc Legros, Jean-Charles Stinville

► **To cite this version:**

Damien Texier, Julien Milanese, Malo Jullien, Julien Genee, Jean-Charles Passieux, et al.. Strain localization in the Alloy 718 Ni-based superalloy: From room temperature to 650 °C. *Acta Materialia*, 2024, 268, pp.119759. 10.1016/j.actamat.2024.119759 . hal-04457558

HAL Id: hal-04457558

<https://imt-mines-albi.hal.science/hal-04457558>

Submitted on 6 Mar 2024

HAL is a multi-disciplinary open access archive for the deposit and dissemination of scientific research documents, whether they are published or not. The documents may come from teaching and research institutions in France or abroad, or from public or private research centers.

L'archive ouverte pluridisciplinaire **HAL**, est destinée au dépôt et à la diffusion de documents scientifiques de niveau recherche, publiés ou non, émanant des établissements d'enseignement et de recherche français ou étrangers, des laboratoires publics ou privés.



Distributed under a Creative Commons Attribution 4.0 International License



Full length article



Strain localization in the Alloy 718 Ni-based superalloy: From room temperature to 650 °C

Damien Texier^{a,*}, Julien Milanese^b, Malo Jullien^a, Julien Genée^a, Jean-Charles Passieux^a, Didier Bardel^c, Eric Andrieu^d, Marc Legros^{e,1}, Jean-Charles Stinville^f

^a Institut Clement Ader (ICA) - UMR CNRS 5312, Université de Toulouse, CNRS, INSA, UPS, Mines Albi, ISAE-SUPAERO, Campus Jarlard, 81013 Albi Cedex 09, France

^b MIDIVAL, 8, avenue Latecoere, 31570 Sainte Foy d'Aigrefeuille, France

^c Framatome, 2 rue Professeur Jean Bernard, 69007 Lyon, France

^d CIRIMAT-UMR CNRS 5085, Université de Toulouse, ENSIACET, 4 Allée Emile Monso, BP 44362, 31030, Toulouse Cedex 4, France

^e Centre d'Elaboration de Matériaux et d'Etudes Structurales, CNRS UPR 8011, 31055 Toulouse Cedex 4, France

^f Materials Science and Engineering, University of Illinois at Urbana-Champaign, USA

ARTICLE INFO

Keywords:

Strain localization
High-resolution digital image correlation
High-temperature
Slip localization
Grain boundary sliding

ABSTRACT

Irreversible deformation in relation to the microstructure was investigated for a polycrystalline Ni-based superalloy (Alloy 718) from room temperature to 650 °C using high-resolution digital image correlation (HR-DIC) techniques. Interrupted tensile tests were performed under a protective atmosphere to ensure the stability of the speckle pattern to track kinematics fields from surface analyses. In-plane strain localization was captured using HR-DIC on scanning electron microscopy (SEM) images. A statistical analysis of different strain localization events in relation to the microstructural features was conducted, *i.e.*, intragranular slip localization, slip localization parallel to and near Σ 3-twin boundaries (Σ 3-TB), and grain boundary sliding (GBS). Alloy 718 exhibited slip localization at room temperature and 350 °C. Intense strain localization develops parallel and in the vicinity of Σ 3-TB from the onset of the microplasticity. Few intense slip stimulated-grain boundary sliding events were found due to slip localization on both grains adjacent to the grain boundary. At 650 °C, Alloy 718 experienced grain boundary sliding at the onset of the yield without particular slip localization in adjacent grains. At lower temperatures, strain localization parallel to and near Σ 3-TB was intense, and intragranular slip localization intensified with increasing macroscopic deformation. Particular microstructural configurations were found at 650 °C leading to premature damage: (i) sub-surface cavitation at grain boundaries, and (ii) grain boundary cracking due to intense shearing near a Σ 3-TB.

1. Introduction

Nickel-based superalloys are commonly used at intermediate and even high temperatures for structural applications in severe atmospheres due to excellent mechanical strength and corrosion/oxidation performance. Alloy 718, also known as Inconel 718, is the most widely used polycrystalline nickel-based superalloy for applications up to 650 °C, such as retention systems on fuel assembly structures in pressurized water nuclear reactors, components for liquid-propellant rocket motors, turbine disks for aeroengines. Some of these applications are critical and require an appropriate description of their mechanical behavior over a large temperature range at the macroscopic scale and their mechanical response at the microstructural scale to better

understand the transition from strain localization to early damage development. Alloy 718 is known to be sensitive to Portevin-Le Châtelier (PLC) effects due to dynamic strain aging (DSA) at intermediate (350–500 °C) and high temperatures (≥ 600 °C) depending on the deformation rate under tensile loading. PLC is more prone to occur at lower temperatures and high strain-rates [1–3] and drastically alters the fracture mode of Alloy 718 from intragranular fracture in the PLC domain to intergranular fracture in the absence of PLC events at intermediate and high temperatures [1–3]. This change in fracture mechanisms as a function of PLC occurrence questions the role of strain localization at the microstructure scale and, more particularly, the

* Corresponding author.

E-mail address: damien.texier@mines-albi.fr (D. Texier).

¹ Marc Legros was an Editor of the journal during the review period of the article. To avoid a conflict of interest, Marc Legros was blinded to the record and another editor processed this manuscript.

<https://doi.org/10.1016/j.actamat.2024.119759>

Received 19 October 2023; Received in revised form 7 February 2024; Accepted 12 February 2024

Available online 13 February 2024

1359-6454/© 2024 The Authors. Published by Elsevier Ltd on behalf of Acta Materialia Inc. This is an open access article under the CC BY license (<http://creativecommons.org/licenses/by/4.0/>).

partitioning between intergranular and intragranular strain localization as a function of the temperature and strain rate.

Developments in high-resolution digital image correlation (HR-DIC) under optical microscopy (OM) [4–6], scanning electron microscopy (SEM) [7–21] or Laser Scanning Confocal Microscopy (LSCM) [22–24] offer the possibility to quantitatively evaluate elementary intragranular deformation mechanisms at room temperature. Strain localization into individual slip bands can be identified on the surface of samples and correlated with EBSD analysis to identify the active slip plane, or even the active slip system by analysis of the projected cumulative Burgers vector [20,23,25,26]. Alloy 718 and other polycrystalline Ni-based superalloys have been studied under tensile loading using HR-DIC at room temperature to categorize different strain localization events as a function of microstructural features, *i.e.*, slip activity in the vicinity of twin boundaries (TB) or grain boundaries (GB) or intragranular slip far from these features [16,20,21,23,27–29]. Particular crystallographic configurations, *i.e.* twins and parent grains oriented in such a way as to exhibit a significant difference in elastic behavior in the main direction of mechanical loading, were identified to concentrate elastic deformation [16]. These microstructural configurations lead to early slip activity at higher deformation levels, without a high Schmid factor (slip system $\{111\} \langle 110 \rangle$), where the Schmid factor is calculated according to the macroscopic loading direction. Slip activity, therefore, develops close to and parallel to the twin boundaries and is generally referred to as parallel slip configuration. Statistical analysis of numerous twin boundaries has revealed configurations that are more or less prone to crack initiation under cyclic loading, depending on the deformation amplitude of the specimens [30]. Stinville et al. [30] defined a crack initiation density function based on a representation of the elastic modulus difference between the parent grain and the twin as a function of the macroscopic Schmid factor. Two evidenced two hotspots of high population density, corresponding to a grain configuration with a high elastic difference but a low Schmid factor and, conversely, a low elastic difference and a high Schmid factor. Slip localization occurs predominantly parallel to and near specific twin boundaries, and the slip intensity is maximal at low levels of deformation, *i.e.* below the yield strength [23]. As plastic loading progresses, intragranular planar slip density increases, but slip intensity remains highest in the vicinity of microstructural singularities such as twin boundaries [23]. Sub-surface characterization of the microstructure beneath the region of interest investigated using HR-DIC aimed to demonstrate that the genesis of intense slip bands is particularly propitious in the vicinity of triple junction in the volume [28].

The application of digital image correlation at small scales has been extended to high temperature, both *in-situ* and *ex-situ* with the scanning electron microscope [10,11,31–37]. Generally, these experiments were carried out in environments that limit the evolution of the surface reactivity of the speckle pattern, as required for digital image correlation. Some tests were performed in air, either for relatively short high-temperature exposure times [31,38], or at temperatures limiting external oxide growth [34]. In the latter study, a γ - γ' polycrystalline nickel-based superalloy was subjected to fatigue and tensile loading at 650 °C. It highlighted intense slip activity in the vicinity of and parallel to the twin boundaries in the early stage of deformation. At this temperature, intragranular planar slip was still dominant for this material, and slip system analyses show the possible contribution of cross-slip. Grain boundary slip has not been demonstrated for this superalloy at this temperature. The performance of microgrid or HR-DIC *in-situ* under SEM was demonstrated on similar materials up to 750 °C, but in protective atmosphere [10,11,35,39,40]. Beyond the technical prowess of these tests, these studies highlighted plastic deformation localizations different from those observed at room temperature, such as plastic activity near grain boundaries or grain boundary sliding [11,36,39].

The present paper focuses on capturing and understanding strain localization events at the microstructure scale in Alloy 718 at temperatures ranging from room temperature to 650 °C using high-resolution

digital image correlation techniques. Strain partitioning, corresponding to the proportion of in-plane strain intensity for classified microplasticity events, *i.e.*, intragranular slip, slip localization in parallel slip configuration, and grain boundary sliding, over the whole strain localization events, was quantified at different temperatures via correlative data between strain maps and EBSD maps.

2. Material and experimental methods

2.1. Material

The material used in the present study was a rolled Alloy 718 Ni-based superalloy sheet of 270 μm with the nominal composition as follows: Ni–18.5Cr–18.3Fe–5.0(Nb+Ta)–3.0Mo–1.0Ti–0.6Al–0.03C (wt. %). Flat dogbone-shaped tensile specimens were machined from the sheet in the transverse direction by a laser-cut stencil technique. Specimens were then heat treated at 1080 °C for 1 minutes under vacuum, then quenched. The standard strengthening treatment was performed to form appropriate γ'' - γ' - γ metallurgical state : a temperature ramp of 5 °C.min⁻¹; temperature dwells at 720 °C for 8 h then at 620 °C for 8 h. A cooling rate of 50 °C h⁻¹ was carried out between 720 and 620 °C and a furnace cooling after 620 °C. The resulting mean grain size was evaluated at 35 μm (excluding twins), and the corresponding microstructure is depicted in Fig. 1. The material presented a weak texture along the transverse direction and no particular grain misorientation except $\Sigma 3$ twin boundaries.

2.2. Tensile testing under protective atmosphere

Flat dogbone-shape specimens have a geometry illustrated in Fig. 2(a) and a thickness of $267 \pm 1 \mu\text{m}$. Before mechanical testing, specimen edges were ground with a P1200 SiC paper to remove the thermally affected region due to the laser-cut stencil technique and residual stresses. The gage section was then electro-polished with 10 % perchloric acid in a methanol solution at 20 V for 5 s for further electron backscattered diffraction (EBSD) characterizations. After EBSD mapping, specimens were slightly oxidized at 650 °C for 15 min in air then 15 min under vacuum ($1.2 \cdot 10^{-5}$ mbar) to produce a fine speckle pattern compatible with high resolution-digital image correlation techniques. The speckle pattern results from differential oxidation of γ (medium gray background), γ' (dark gray dots), and γ'' precipitates (white dots) and is depicted in Fig. 1(a),(c) and (d).

Tensile experiments were conducted at room temperature, 350 °C, and 650 °C with a MTS Criterion model 43 electromechanical test system equipped with a 5 kN load-cell and a radiative furnace (MTS-653.04 model) under air for monotonic tests up to fracture and in an ultra-high vacuum quartz chamber for interrupted tensile tests. The temperature was controlled at three locations using R-type thermocouples. A vacuum of $2.5 \cdot 10^{-5}$ mbar was reached before each high-temperature interrupted test. Baking at 150 °C for 20 min was done before the temperature ramp to reduce water and oxygen physisorption due to chamber opening to limit oxidation further. A pre-load of 20 MPa was applied during heating, and tensile tests were performed under constant cross-head displacement ($2.5 \mu\text{m s}^{-1}$, *i.e.*, a strain rate of approx. $7.9 \cdot 10^{-5} \text{ s}^{-1}$) after the thermal stabilization of 5 min at the testing temperature. For monotonic tests under air, contact extensometry was used for direct measurement of the specimen deformation. For interrupted tests under vacuum, specimens were measured before and after each tensile interruption with a caliper and an apochromatic zoom microscope.

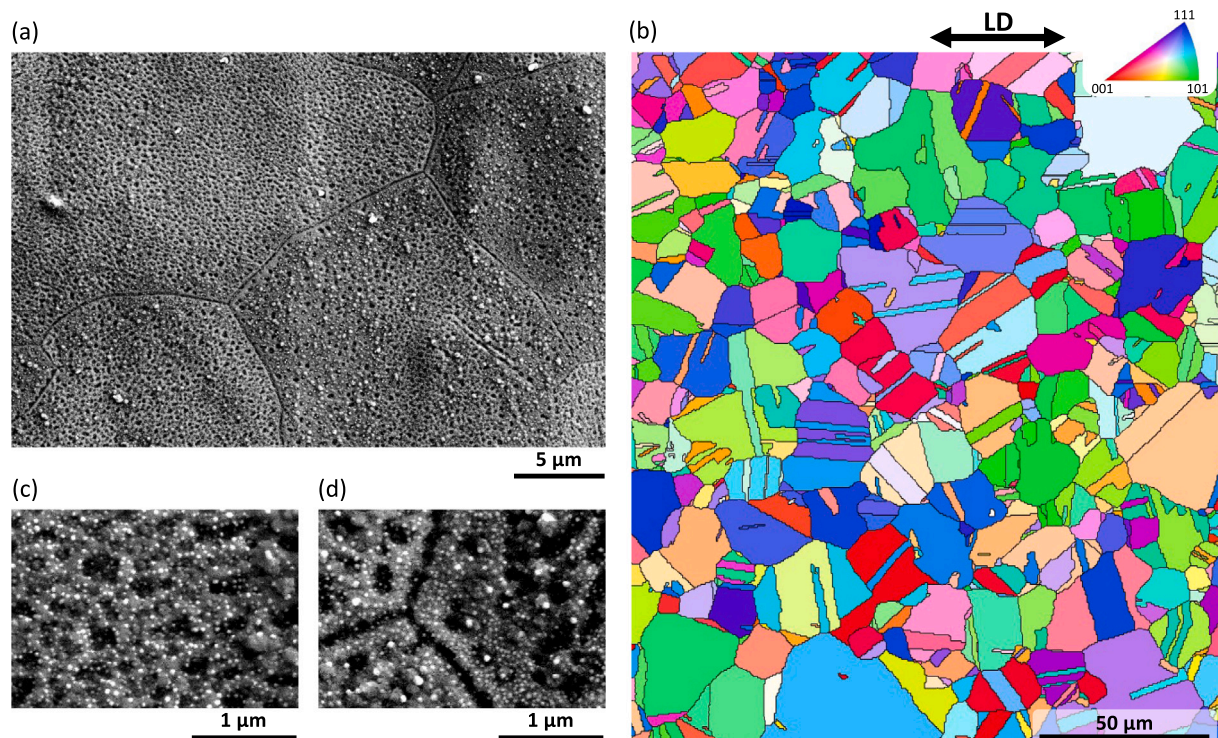


Fig. 1. Illustration of the microstructure and speckle pattern at different scales. (a) Scanning electron micrograph showing the speckle pattern and the grain structure. (b) Inverse pole figure (IPF) map in reference to the loading direction (LD) showing the grain structure and weak texture. (c) and (d) Speckle pattern in the grain core and the vicinity of grain boundaries. (For interpretation of the references to color in this figure legend, the reader is referred to the web version of this article.)

Table 1

DIC hardware parameters.

Camera manufacturer	ThermoFischer scientific/Everhart-Thornley detector
Camera Model	Helios 600i/Everhart-Thornley detector
Electronic column	Elstar FEG Schottky
Image Resolution	3072 × 2048 (7 × 7 mosaic with 20 % overlap)
FOV	31.75 × 21.17 μm ²
Image Scale	10.3 nm/pixel
Acceleration voltage	10 keV
Probe current	0.69 nA
Working distance	5 mm
Dwell time	20 μs
Patterning technique	15 min oxidation at 650 °C
Approx. pattern feature size	3.6 pixel

2.3. High resolution-digital image correlation (HR-DIC) using a scanning electron microscope (SEM)

High resolution-digital image correlation (HR-DIC) was performed *ex-situ* using a field emission gun-scanning electron microscope (FEG-SEM). The microscope was a Helios 600i from ThermoFischer Scientific with an Elstar high-resolution electronic column (FEG Schottky). A mosaic of 7 × 7 micrographs with an overlap of 20 % was collected before and after tensile interruptions in order to obtain the in-plane kinematics field for each deformation step. Micrographs were acquired with a resolution of 3072 × 2048 pixels with a horizontal field of view of 31.75 μm. FEG-SEM parameters were: an acceleration voltage of 10 keV, a probe current of 0.69 nA, a working distance of 5 mm, and a dwell time of 20 μs. Specimen alignment was done by iterative rotation corrections for finding the horizontality of specimen edges from head to head using the linear stage of the SEM. The acquisition parameters are summarized in Table 1, as advised by Ref. [41].

The optical flow algorithm was first used to assess regularized displacement fields [42,43]. The finest level of the multi-scale pyramid on which the optical flow was computed is equal to 1, the weight of the smoothness term is 20, the weight of the color constancy term is 5,

and the weight of the gradient constancy term is 10. Five iterations of variational refinement were performed per scale with a patch size of 8 and a patch stride of 3. Kinematics fields using optical flow techniques were only used for visual representation of the in-plane strain fields according to the loading direction. Heaviside-DIC (H-DIC) [20,44] was also applied on the different datasets to capture better discrete microplasticity, *i.e.*, slip activity, grain boundary sliding, etc. at the microstructure scale. H-DIC is capable of measuring sub-pixel jumps; minimal in-plane slipping/sliding amplitude clearly evidenced from H-DIC were of 0.4 pixel (4 nm or about tens of dislocations). Discontinuity thicknesses up to 7 pixel (70 nm) maximum were observed. In other words, the H-DIC technique, based on the quality of this speckle pattern for high temperature, was capable of dissociating strain localization separated by 2 times this discontinuity width, *i.e.*, 140 nm. This spacing is relatively small compared to the one observed in the present study (at least micrometers). Strain localization events were manually segmented for each specimen (up to 914, 1014, and 1597 events at room temperature, 350 °C and 650 °C). Events were then automatically classified into three categories, *i.e.*, intragranular slip, slip near and parallel to twin boundary and grain boundary sliding, based on morphological considerations and position related to the microstructure (proximity

Table 2
DIC analysis parameters using the optical flow technique [42] and the Heaviside-DIC (H-DIC) technique.

	Optical flow	H-DIC
Subset Size	8 pixels	41 pixels
Step Size	3 pixels	3 pixels
Subset Shape Function	Rigid	First gradient - Heaviside
Interpolant	Bilinear	Bicubic
Matching criterion	Zero-normalized sum of square differences (ZNSSD)	-
Number of pyramidal scales	5	-
Variational refinement	$\sigma=20, \gamma=10, \alpha=5$	-
Strain step	7 pixels	3 pixels

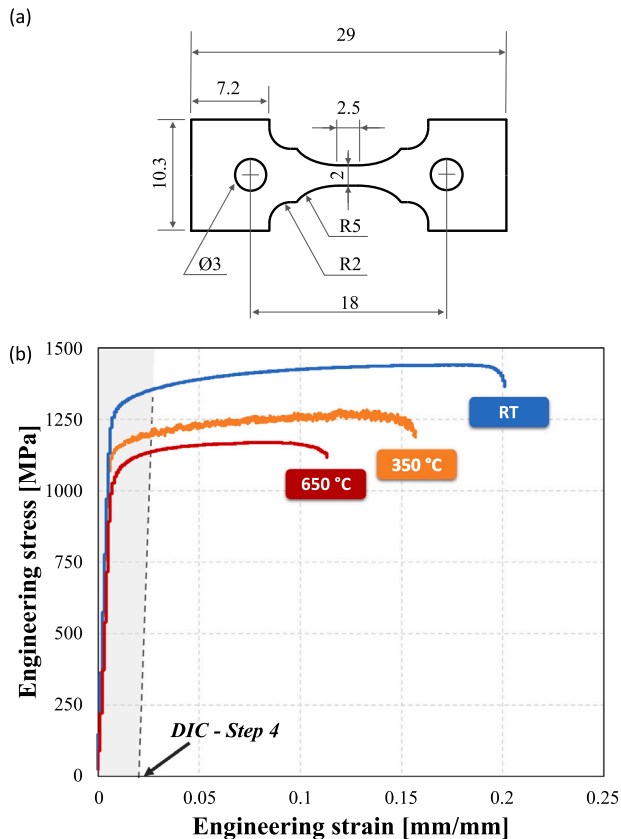


Fig. 2. (a) Geometry of the tensile specimens (dimensions in mm). (b) Stress-strain curve of Alloy 718 at room temperature, 350 °C and 650 °C.

to twin boundaries or grain boundaries. The maximal distance from the twin boundary or grain boundary was considered of 1 μm (100 pixels)). H-DIC measurements allow the statistical analysis of in-plane slip amplitude for each category of slip events [45]. DIC analysis parameters using either the optical flow algorithm or H-DIC techniques are reported in Table 2.

2.4. Additional characterization techniques

EBSD characterizations were performed before speckle pattern application using a JEOL JSM 7100F scanning electron microscope equipped with a CMOS Symmetry S1 EBSD detector (Oxford Instruments). EBSD maps of 500 \times 250 μm were acquired with a square grid of 0.5 μm in order to obtain the average orientation per grain. This characterization is important to correlate microplasticity to local microstructure and crystallographic features. Kernel average misorientation (KAM) representations were also calculated using a circular pattern with a radius of 5 pixels to evidence crystallographic lattice curvatures.

Height maps were acquired using laser scanning confocal microscopy (LSCM) on the different tensile specimens after the last DIC loading to capture out-of-plane information from height map measurements. The microscope was a LEXT Olympus OLS5100 equipped with a 405 nm wavelength laser. High-resolution topographic measurements were performed using a MPLAPON100XLEXT lens and image resolutions of 4096 \times 4096 pixels. The step size of 120 nm allows a resolution of 12 nm. Height difference calculations detailed in Ref. [23,46] were applied to further combine out-of-plane and in-plane discontinuity events and relate them to the microstructure. These results are shown in **supplementary material** due to insufficient initial topography using electrochemical polishing.

Small focused-ion-beam (FIB) cross-sections were performed using a Helios 600i dual-beam microscope from ThermoFischer Scientific with a Tomahawk ionic column. Large FIB cross-sections were performed using a Lyra3 dual-beam microscope from TESCAN to document grain morphology, deformation, and damage features in the sub-surface region.

3. Results

3.1. Macroscopic tensile behavior at the different temperatures

Monotonic tensile tests were performed at room temperature, 350 °C and 650 °C under air to assess the macroscopic tensile behavior of the Alloy 718 as a function of the temperature. Stress-strain curves are shown in Fig. 2(b). Alloy 718 exhibits a gradual drop of mechanical strength with temperature increase. While the stress-strain response in the plastic domain is relatively smooth at room temperature and 650 °C, the occurrence of Portevin-Le Chatelier (PLC) events, materialized as jerky flow and stress drops, was found at 350 °C. The 0.2% yield strength of Alloy 718 was of 1282, 1143, and 1056 MPa at room temperature, 350 °C and 650 °C, respectively. The material has a moderate strain hardening behavior in this temperature range. Interrupted tensile tests were then conducted with HR-DIC to document microplasticity events at different deformation stages for the three temperatures.

3.2. Surface observation of the microplasticity and texture pattern evolution

Tensile specimens were observed using a FEG-SEM after each interruption in order to observe microplasticity development at the surface, early damage development, and surface texture evolution. Some recurrent microplasticity events are shown in Fig. 3 for the different temperatures. At room temperature and 350 °C, slip localization is the prominent deformation mechanism observed at the specimen surface. Most intense and out-of-plane slip events appear as white bands across grains, with potential effects on the algorithm convergence for further HR-DIC calculations. Slip event density evaluated using slip trace analysis is relatively low compared to prior HR-DIC measurements performed on similar materials [23,28]. At 650 °C, intragranular slip was less pronounced but still present. Some modification of the surface texture in the vicinity of grain boundaries seems to highlight strain localization near grain boundary or even grain boundary sliding. Furthermore, the texture pattern, *i.e.*, the gray-level contrast, and features, are conserved

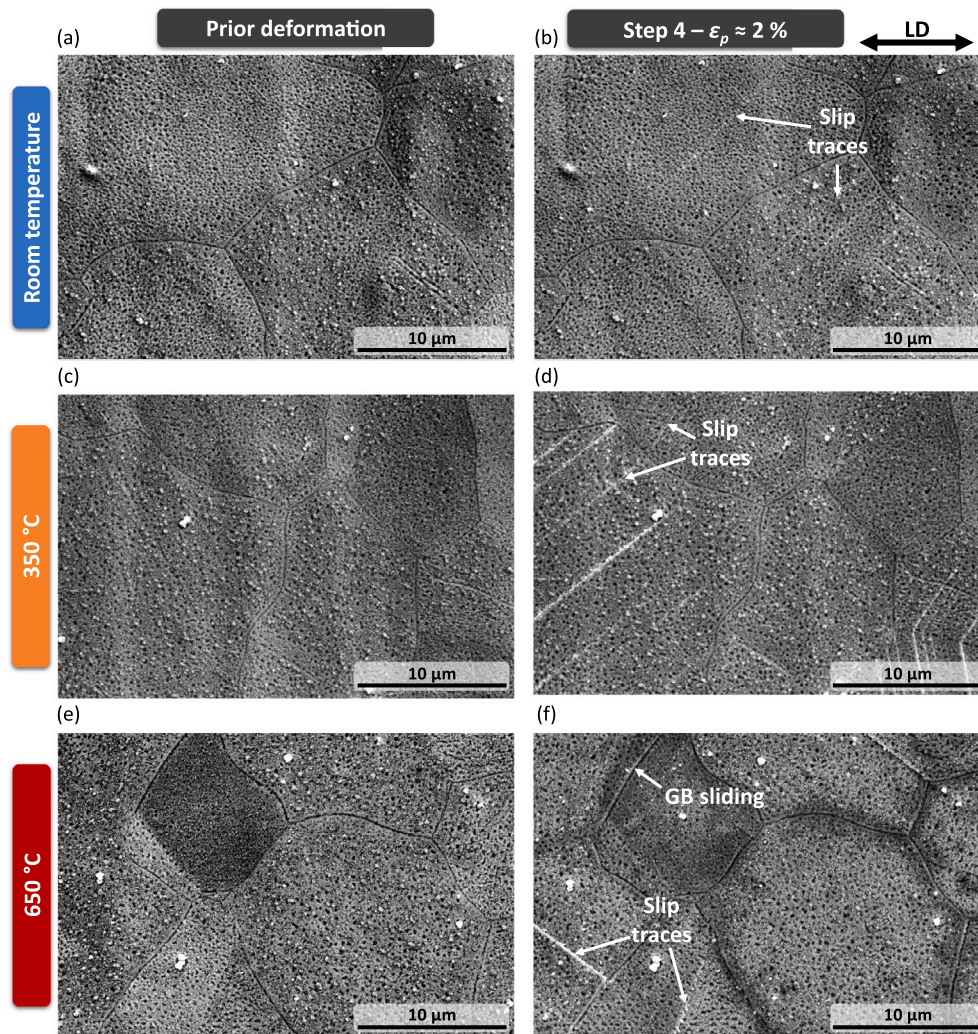


Fig. 3. SEM micrographs in secondary electron mode of specific regions of interests (a), (c), (e) before and (b), (d), (f) after the fourth interrupted tensile step for each temperature: Observation of microplasticity events and texture pattern evolution.

up to 350 °C due to minor oxidation during mechanical testing. However, tests at 650 °C lead to slight surface reactivity due to oxidation (interference color change between two successive tensile interruptions). This optical surface modification also generates modifications of the texture pattern, especially in the vicinity of grain boundaries or the global gray level of given grains. Nevertheless, texture contrast was sufficiently pronounced and stable to allow for HR-DIC calculations.

3.3. Microplasticity events at room temperature using HR-DIC

HR-DIC was performed using *ex-situ* FEG-SEM micrographs to evaluate the in-plane kinematic fields of the specimen after different deformation steps at room temperature. Fig. 4(a) depicts the grain structure and orientation of the region of interest. All the tensile interruptions were performed in the macroscopic plastic regime, the first step being at 0.1% plastic strain. At such a low deformation level, the most intense microplasticity events were associated with slip localization parallel to and near twin boundaries, as depicted by black and green arrows in Fig. 4(a) and (b), respectively. Intragranular slip events and strain localization events in the vicinity of grain boundaries (GB) were also observed. For microplasticity near GB, no particular intragranular activity was found in grains adjacent to these GB events (white and green ellipses in Fig. 4(a) and (b) respectively). Slip activity parallel to and near TB was found to interact with microplasticity near GB (one event),

but a larger region of interest would be necessary to confirm such a stochastic interaction. At higher plastic strain, intense intragranular slip activity develops and, in some cases, induces strain localization in the vicinity of grain boundaries (as indicated by white and red ellipses in Fig. 4(a) and (d)). This is referred to as slip-stimulated grain boundary sliding (SSGBS), and shows the importance of intragranular slip activity adjacent to a grain boundary to have stress accumulation and grain boundary sliding, as referred in Ref. [47]. This mechanism mainly developed at 1.9% macroscopic plastic strain. Slip localization parallel to and near TB appeared particularly intense regardless of the macroscopic strain level.

3.4. Microplasticity events at 350 °C using HR-DIC

Similar analyses were performed at 350 °C to depict microplasticity events at the microstructure scale (Fig. 5). Despite the occurrence of PLC, microplasticity was found very comparable to the one at room temperature, *i.e.*, (i) intense slip localization parallel to and near TB regardless of the macroscopic strain level, (ii) an increase in intragranular slip events with the macroscopic plasticity, (iii) development of SSGBS with the macroscopic plasticity. Statistical analyses of the slip activity will aim at a quantitative distinction in microplasticity partitioning at the grain level between room temperature and 350 °C.

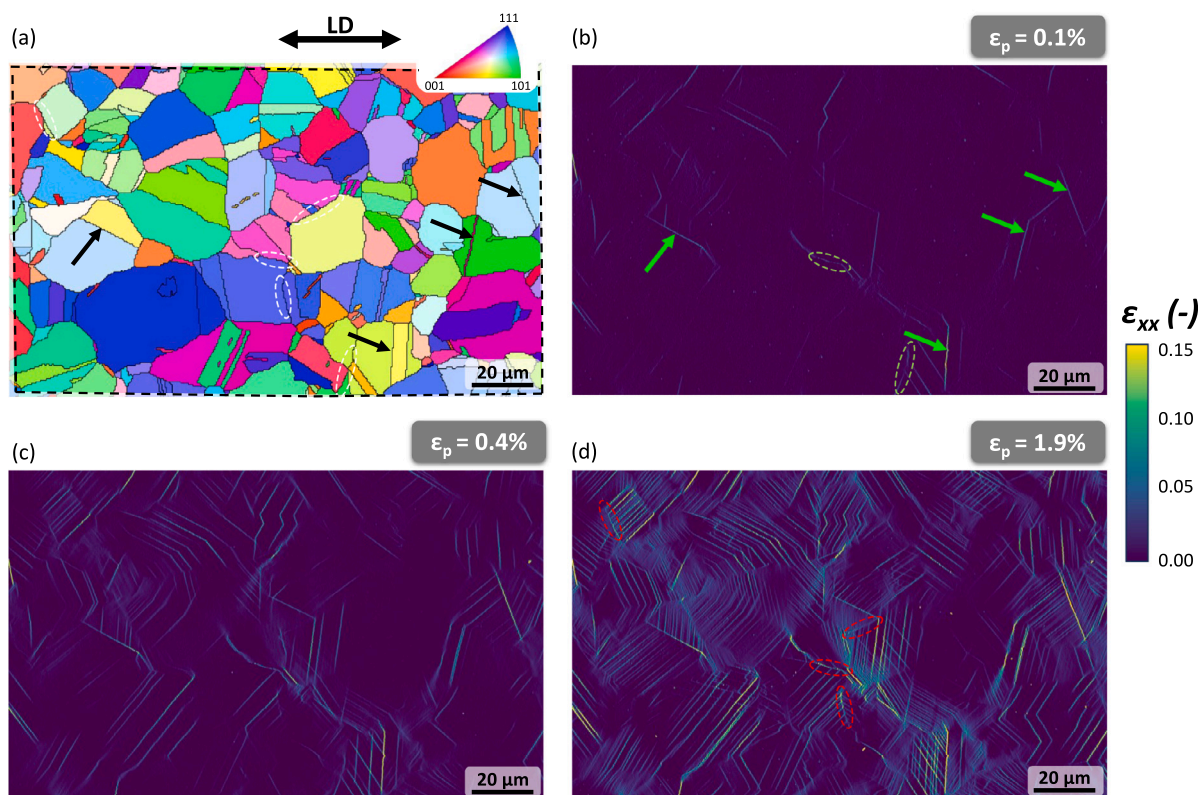


Fig. 4. Region of interest and strain maps at different macroscopic plastic strain levels at room temperature. (a) IPF map in reference to the loading direction (LD). In-plane deformation along the principal loading direction at (b) 0.1% plastic strain, (c) 0.4% plastic strain, and (d) 1.9% plastic strain. Arrows and ellipses aim at highlighting particular microplasticity events. (For interpretation of the references to color in this figure legend, the reader is referred to the web version of this article.)

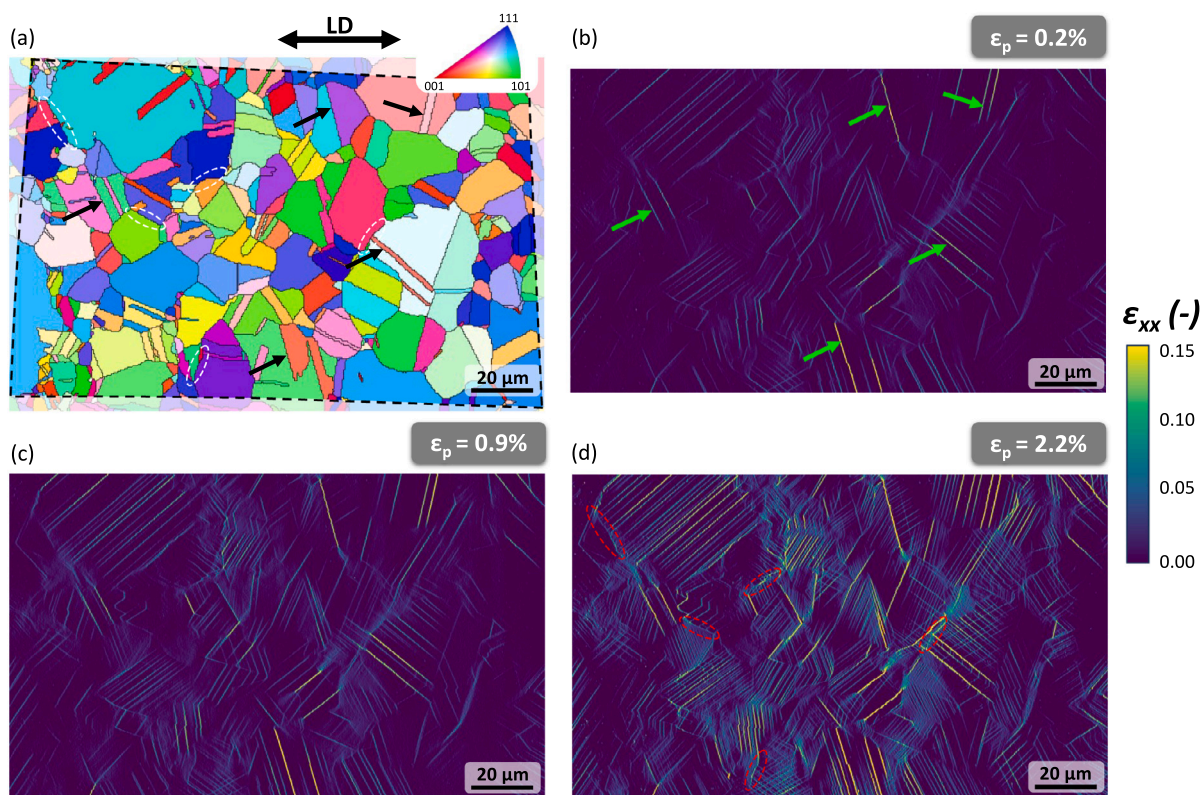


Fig. 5. Region of interest and strain maps at different macroscopic plastic strain levels at 350 °C. (a) IPF map in reference to the loading direction (LD). In-plane deformation along the principal loading direction at (b) 0.2% plastic strain, (c) 0.9% plastic strain, and (d) 2.2% plastic strain. Arrows and ellipses aim at highlighting particular microplasticity events. (For interpretation of the references to color in this figure legend, the reader is referred to the web version of this article.)

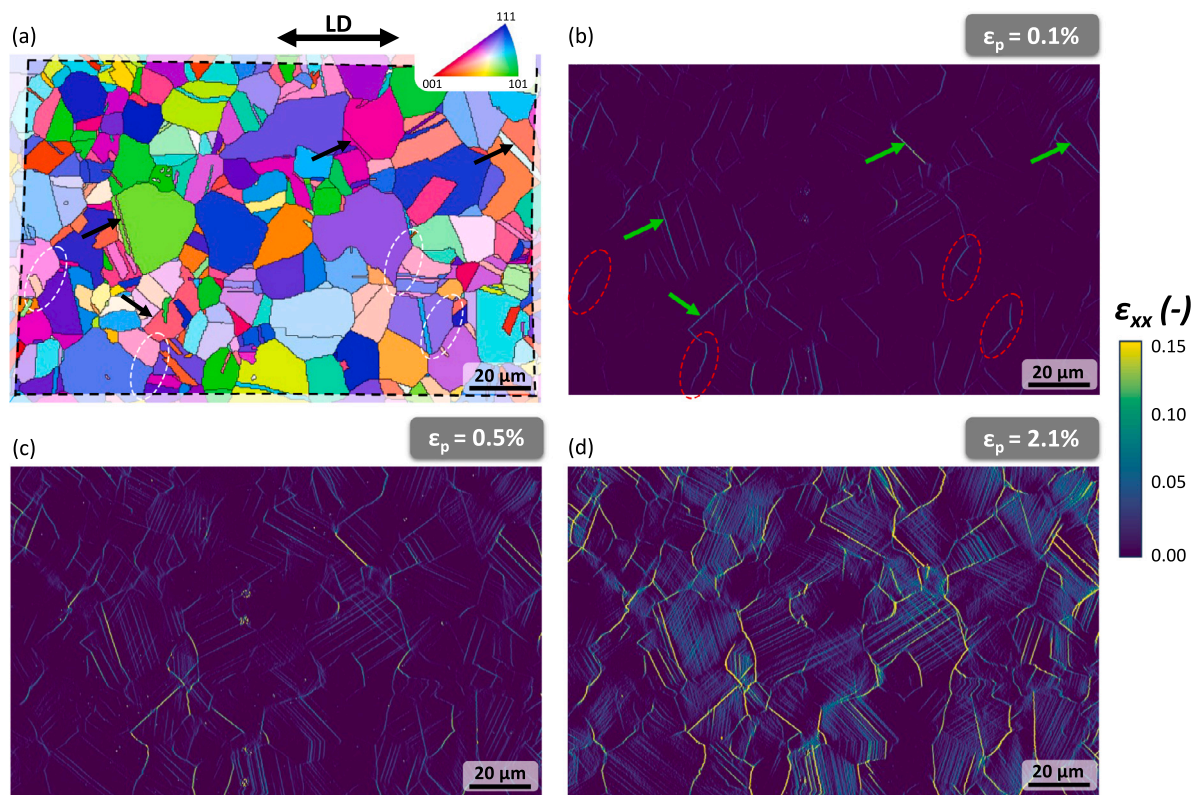


Fig. 6. Region of interest and strain maps at different macroscopic plastic strain levels at 650 °C. (a) IPF map in reference to the loading direction (LD). In-plane deformation along the principal loading direction at (b) 0.1% plastic strain, (c) 0.5% plastic strain, and (d) 2.1% plastic strain. Arrows and ellipses aim at highlighting particular microplasticity events. (For interpretation of the references to color in this figure legend, the reader is referred to the web version of this article.)

3.5. Microplasticity events at 650 °C using HR-DIC

HR-DIC measurements were also performed at 650 °C (Fig. 6). Interestingly, strain partitioning at the microstructure scale was found to be different from tests performed at low and intermediate temperatures, even at the onset of microplasticity. Strain localization in the vicinity of grain boundaries was found at 0.1% plastic strain without particular interaction with slip activity in adjacent grains (white and red ellipses in Fig. 6(a) and (b)). Strain localization parallel to and near TB was also particularly intense. Grain boundary sliding (GBS) and intragranular slip events multiply and grow in intensity as deformation increases. Most intense in-plane strain localization events are found at grain boundaries and twin boundaries, regardless of the loading step.

HR-DIC using an SEM inform on the in-plane components of the kinematic fields. Post-mortem topographic measurements were performed on the final deformation step using a laser scanning confocal microscope to evaluate height steps on the surface. The readers should refer to **supplementary material** for additional details.

3.6. Early damage development at 650 °C from surface observations and HR-DIC

While the region of interest (ROI) for each HR-DIC measurement corresponds to a small region of the specimen gage, the whole gage region was inspected under SEM for each tensile interruption. No particular crack was observed at RT and 350 °C up to 2 % plastic strain. However, few cracks at grain boundaries or evidence of grain boundary sliding were observed for tests at 650 °C out of the HR-DIC ROI only at the 4th loading step (Fig. 7). Few FIB notches were machined at grain boundaries in order to document grain boundary sliding. Shearing of such features highlighted the concomitant action of twin boundary sliding and grain boundary sliding at a high temperature

(Fig. 7(b)). Gray-level contrast in the vicinity of GB, resulting from edge effects, also demonstrates the necessity to acquire out-of-plane kinematics fields to predict better grain boundary sliding.

Twin boundary/grain boundary interactions were also found to occur in the sampled ROI. The evolution of strain localization from the 3rd to the 4th step of a particular region is illustrated in Fig. 8 along with the corresponding SEM micrographs. Slip localization parallel to and near the twin boundary develops first following the $[101](1\bar{1}1)$ active slip system (see e.g. Fig. 6 for previous deformation steps). This slip localization imposes an intense shearing along the twin plane with an initial in-plane slip direction nearly 15° off the slip trace. This angle decreased to 10° once grain boundary sliding occurred at the extremity of the twin boundary. For information, the out-of-plane component of the identified Burgers vector is 45° off compared to the sample surface. This intense slip localization subsequently activated grain boundary sliding (Fig. 8(a) and (b)) then cracking for larger deformation (Fig. 8(c) and (d)). This configuration clearly demonstrates the concomitant action of particularly intense slip localization along TB leading to early damage in adjacent grain boundaries.

3.7. Early damage development at 650 °C in the sub-surface

Cross-sectional observations were conducted to document the sub-surface microstructure and potential damage development in the volume. A large FIB-machined cross-section was performed on the HR-DIC ROI after 2.1 % plastic strain. The dashed lines in Fig. 9(a) and (b) correspond to the location of the FIB cross-section. EBSD analyses on the cross-section evidenced high lattice curvature at some grain boundary locations, i.e., near the surface and in the volume. A particular location near the specimen surface was highlighted in Fig. 9 by a white arrow based on the occurrence of high lattice curvature and pores located at the grain boundary (Fig. 9(e-f)). Grains adjacent to this grain

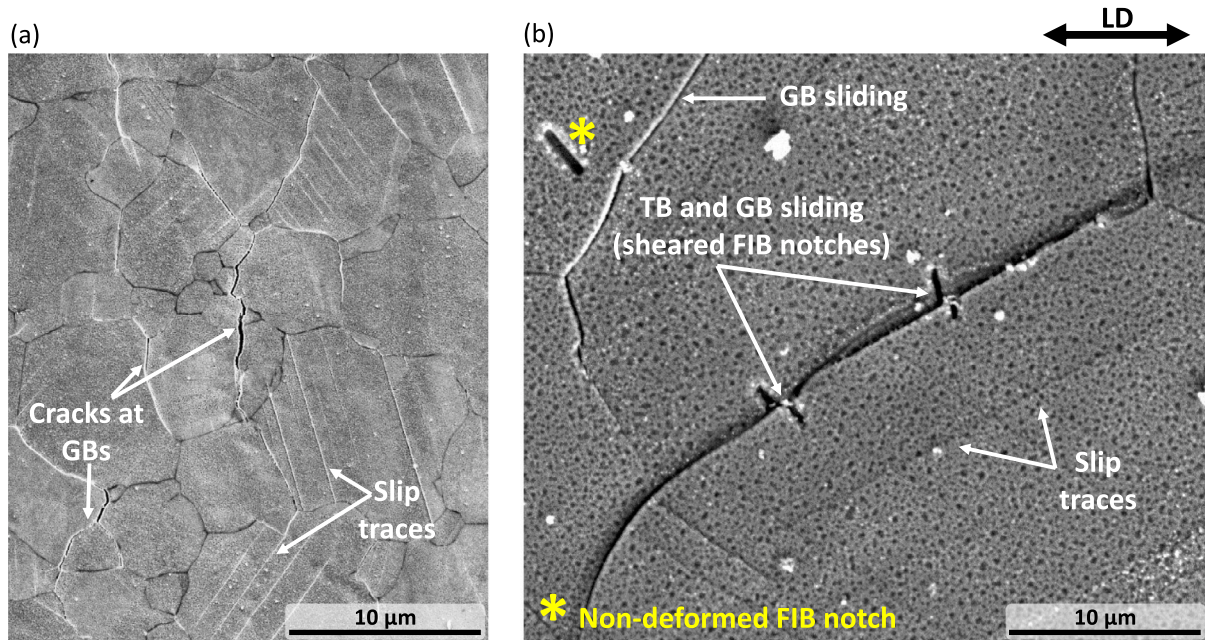


Fig. 7. Early damage development at 650 °C, i.e., grain boundary sliding and GB cracking. (a) Region showing mainly GB cracking, (b) Interaction of slip at TB and GB sliding highlighted by shearing of FIB notches machined before deformation.

boundary have the following characteristic: loading direction being mainly aligned with $\langle 001 \rangle$ in one grain, and with $\langle 011 \rangle$ in the other one (see e.g. Fig. 9(c)). SEM micrographs in backscattered electron (BSE) mode depict the presence of pores located at the grain boundary, corresponding to cavitation and height steps relative to the out-of-plane sliding at the grain boundary. Such damage was not connected to and visible from the surface. H-DIC measurements are aimed at measuring the angle between the displacement jump direction associated with this grain boundary sliding as a function of the grain boundary trace at the surface. Interestingly, the displacement jump is nearly perpendicular to the grain boundary (82.5° and 85.5°). When closely looking at the microstructure leading to cavitation, some interesting features are observed, such as (i) high elastic difference due to crystal orientation, (ii) grain boundary nearly orthogonal to the loading direction both at the surface and in the cross-section, (iii) sub-surface strain localization evidenced by high KAM values, (iv) intense slip localization at a TB in the neighborhood, (v) several slip bands in adjacent grains. It is worth mentioning that the in large FIB-machined cross-section, cavitation is sparsely distributed and corresponds to 1 event for 15 grain boundaries emerging at the surface. No cavitation was found below $3 \mu\text{m}$ beneath the surface. The angle between the displacement jump and the grain boundary trace at the surface ranged from 1.2° to 45.5° for grain boundaries having no cavitation. Additional analyses on larger volume would be necessary to better document the origin of cavitation and microstructural configurations avoiding it.

Another region of interest was investigated with an inclined cross-section orientation compared to the loading direction for two grain boundaries presenting similar inclination traces and strain localization from surface observation (Fig. 10). A Pt layer was deposited onto the region of interest using electron then Ga source to avoid curtaining effects and rounded edges during the cross-section FIB machining (gray rectangle in Fig. 10(d)). The FIB-machined cross-section revealed the sub-surface microstructure, and more particularly pores, i.e., cavitation along the grain boundary on the right-side grain boundary, but not on the left one (Fig. 10(e) and (f)). Alignment of distinct pores decorated the grain boundary down to $2 \mu\text{m}$ beneath the external surface and did not emerge at the surface. As aforementioned, the grain boundary experiencing cavitation is nearly vertical in the volume, compared to the second grain boundary. The angle between the displacement jump

and the grain boundary trace at the surface is 82.6° for the grain experiencing cavitation and 52° for the grain boundary having no cavitation. Therefore, morphological considerations of grains have to be considered for damage development along grain boundary as well as the orientation of the sliding direction compared to the grain boundary surface.

Cross-sectional observations aimed at evidencing cavitation at high temperature occurring for some grain boundaries, but surface strain localization does not necessarily lead to pores formation in the volume (Fig. 11). FIB-machined cross-section combined with EBSD measurements aimed at depicting grain boundaries with relatively high lattice rotation in the volume developing in their vicinity but no cavitation in the volume. For information, the angles between the displacement jump and the grain boundary trace at the surface are 46° and 54° . Small surface cracks were yet observed (approx. 250 nm -long cracks). Furthermore, slip at TB in the volume also favored large lattice rotation in adjacent grains due to strain incompatibility from grain to grain (black arrows in Fig. 11(c) and (d) for instance), generally called “micro-volumes” in the literature [48,49]. KAM maps also highlighted maximal lattice rotation in the vicinity of grain boundaries for several grains in the volume.

3.8. Classification and statistical analyses of strain localization events

Data registration then merging using deformation maps (strain maps, in-plane displacement jump, in-plane slipping/sliding direction) and EBSD maps, aimed at classifying the different strain localization events as a function of the microstructure, similarly to Refs. [23,28]. For information, up to 914, 1014, and 1597 events were identified for the last deformation steps at room temperature, 350°C and 650°C , respectively. Strain localization was categorized into events occurring in the vicinity of grain boundary (grain boundary sliding), in the vicinity of twin boundaries, or in an intragranular manner. This classification aimed at calculating strain partitioning at the microstructure scale, i.e., the proportion of in-plane strain intensity for intragranular slip, slip localization in parallel slip configuration, and grain boundary sliding over the whole strain localization events. At room temperature, the fraction of intragranular slip is particularly important and increases with the plastic strain at the expense of twin boundary events and

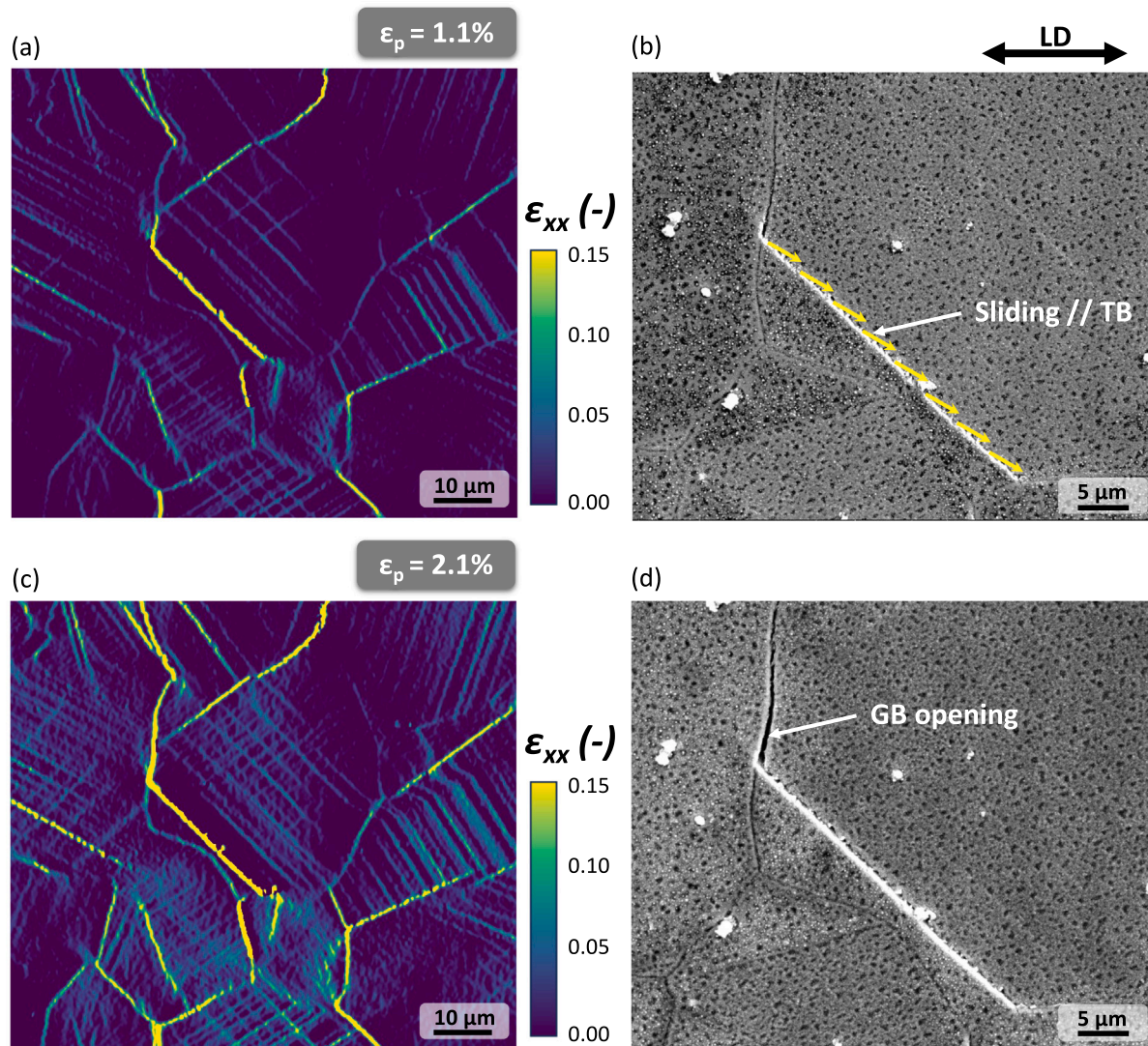


Fig. 8. Interaction between intense slip activity parallel to and near twin boundaries at 650 °C leading to (a), (b) grain boundary sliding at 1.1 % plastic strain, then (c), (d) grain boundary opening at 2.1 % plastic strain. (For interpretation of the references to color in this figure legend, the reader is referred to the web version of this article.)

grain boundary events (Fig. 12(a)). Such a deformation mechanism significantly contributes to strain partitioning in the overall deformation (Fig. 12(d)). Even if the number of strain localization events at grain boundaries increased at a larger deformation level due to the occurrence of slip-stimulated grain boundary sliding, the development of intragranular slip makes the fraction of grain boundary events decrease with the plastic strain. Interestingly, strain partitioning at TBs is greater compared to its physical occurrence, confirming that slip events parallel to and near twin boundaries bear intense in-plane shearing in the overall deformation. A similar deformation behavior is observed at 350 °C (Figs. 12(b) and (e)). At 650 °C, strain partitioning at the microstructure scale is very different due to the occurrence of intense strain localization at grain boundaries from the early stage of plastic deformation. The fraction of intragranular slip is much lower at similar plastic strain compared to similar events at RT and 350 °C (Figs. 12(c) and (f)). While intragranular slip events increased in number (Figs. 12(c)), strain partitioning depicts that grain boundary sliding remains particularly intense and occupies a large proportion of the overall deformation (Figs. 12(d)). Strain localization at twin boundaries is also greater in strain intensity compared to the occurrence of events, demonstrating relatively high in-plane shearing parallel to and near twin boundaries.

This statistical approach was applied to the 100 most intense strain localization events. Interestingly, stacked bar charts in Figs. 12 and 13 show some different trends. As mentioned, strain localization occurrence and partitioning are similar at RT and 350 °C. Interestingly, strain localization parallel to and near twin boundaries increased in number as well as strain partitioning at the expense of intragranular slip. At 650 °C, most intense events are mainly located in the vicinity of grain boundaries due to the activation of grain boundary sliding. Despite a lower representation of strain localization at twin boundaries compared to grain boundaries (in numbers), greater strain partitioning at twin boundaries highlights that shearing intensity at twin boundaries is particularly intense at this temperature. Additional analyses are also presented in **supplementary material** to highlight the strain distribution for each category.

3.9. Crystallographic and morphological aspects on grain boundary sliding

Grain boundary sliding was found to have a significant contribution to the overall deformation process of Alloy 718 at 650 °C. Therefore, particular attention was paid to grain boundary morphological and crystallographic aspects to document the onset and intensity of grain boundary sliding at different temperatures. The grain boundary

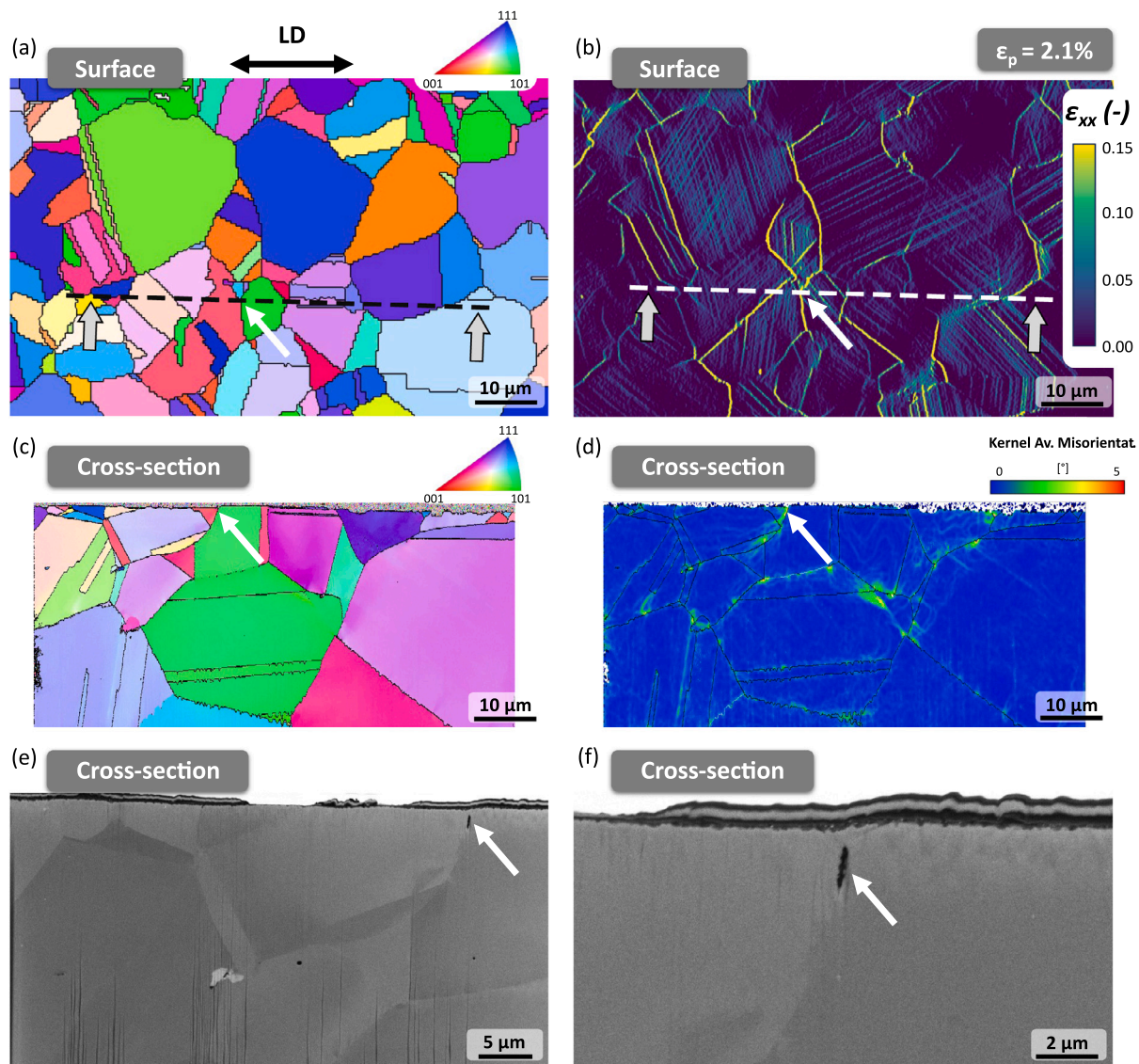


Fig. 9. Sub-surface damage development at 650 °C and 2.1 % plastic strain: cavitation at the grain boundary. (a) EBSD map of the specimen surface. The dashed line corresponds to the FIB cross-section. Gray arrows correspond to the cross-section observation direction. The white arrow highlights the location of a cavitation event. (b) Strain map along the macroscopic loading direction. (c) EBSD map on the cross-section represented as IPF along the loading direction. (d) Kernel average misorientation (KAM) map. (e), (f) SEM image in BSE mode depicting pores after two consecutive FIB slicing, *i.e.*, cavitation. (For interpretation of the references to color in this figure legend, the reader is referred to the web version of this article.)

morphological orientation corresponds to the 2D angle between the loading direction and the grain boundary segment between two triple junctions, as schematically illustrated in Fig. 14(a). Fig. 14(a) to (c) depicts the influence of the grain boundary morphological orientation on the occurrence and intensity of grain boundary sliding at the 4th strain level at RT, 350 °C, 650 °C. The color code corresponds to the deformation step at which the strain localization event at grain boundaries occurs. At room temperature, grain boundary sliding can be activated at low deformation level for morphological inclination ranging from 15° to 82° (dark blue events in Fig. 14(a) and also from 98° to 165° by symmetry), both extreme angles showing maximal in-plane shearing (approx. 400 nm). At the onset of plasticity, strain localization at grain boundary was not necessarily interacting with intense intragranular slip activity on adjacent grains but can interact with intense shearing at twin boundaries (Fig. 4). Events occurring at early deformation levels are generally more intense at the last deformation step than others. However, few events can be relatively intense at the last deformation step due to the development of slip-stimulated grain boundary sliding. The material experienced a similar behavior at 350 °C (Fig. 14(b)). At 650 °C, several strain localization

events at grain boundaries appear from the first deformation levels with sometimes morphological inclination ranging from 1° to 85° (and also 95° to 179° by symmetry). As for RT and 350 °C, the orientation of the grain boundary trace at the surface seems not to be a particular factor influencing grain boundary sliding since its 3D orientation/inclination might be a better morphological parameter. When grain boundaries are inclined according to the loading direction 15 to 75° (modulo 90°), grain boundary sliding is expected. From a morphological standpoint, 90° would favor opening while 0 or 180° should inhibit sliding. These surface considerations related to a macroscopic loading directions are a first approach but does not consider the three-dimension nature of the grain boundary and kinematics field. 90° is not necessarily an “opening” condition since out-of-plane displacement can be observed for such morphological cases. Such considerations refer to a macroscopic loading while strain/stress field at the microscale is highly heterogeneous in nature, making the analysis not so trivial. In addition, slip activity in adjacent grains plays a role and can activate grain boundary sliding regardless of morphological orientation of the grain boundary. For the 0 or 180° configuration, the intense grain boundary

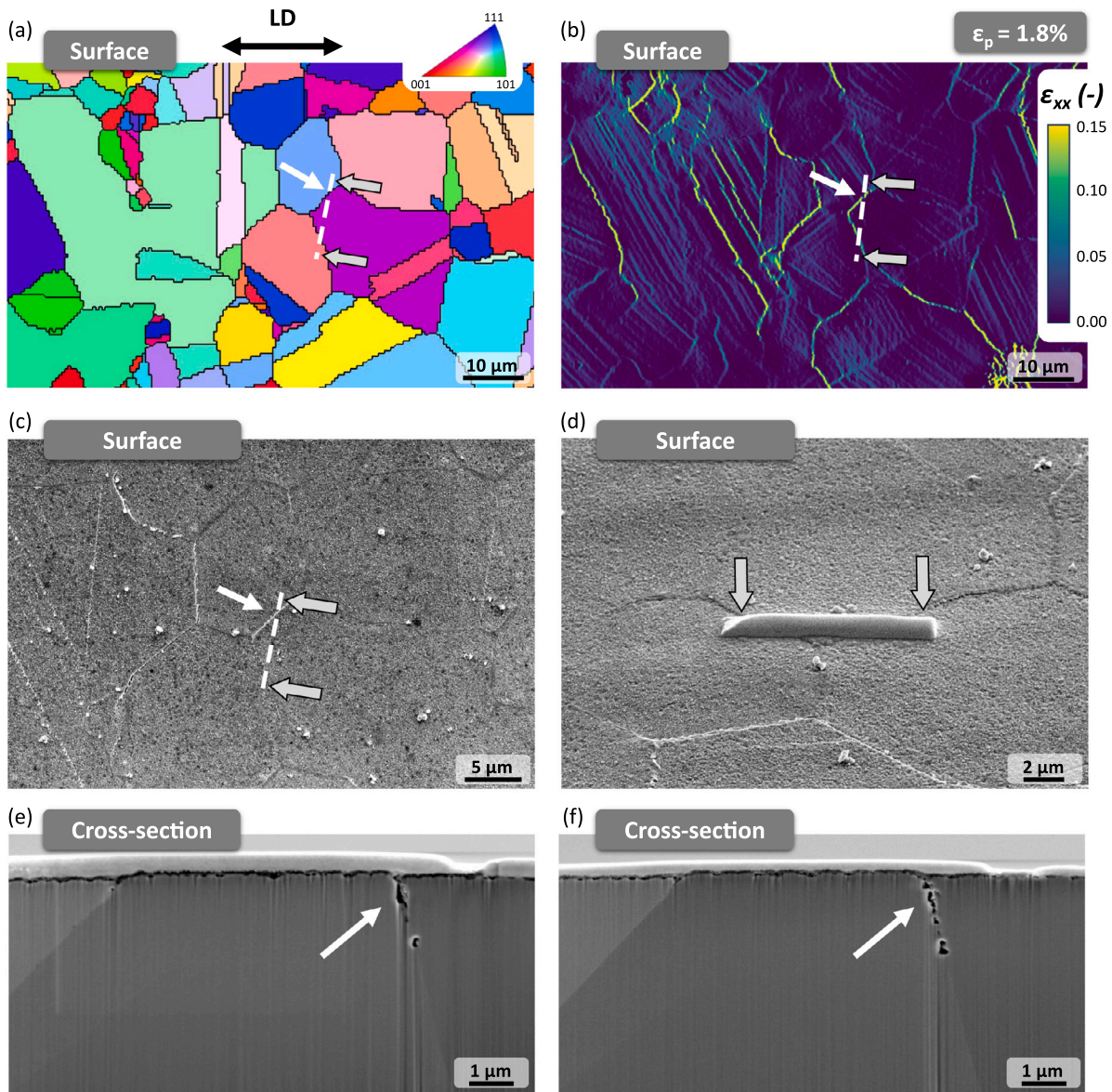


Fig. 10. Sub-surface damage development at 650 °C and 2.1 % plastic strain: cavitation at the grain boundary. (a) EBSD map of the specimen surface. The dashed line corresponds to the FIB cross-section. Gray arrows correspond to the cross-section observation direction. The white arrow highlights the location of a cavitation event. (b) Strain map along the macroscopic loading direction. (c), (d) Surface observation under SEM in SE mode showing no particular cracking/damage at both grain boundaries. (e), (f) Cross-section observations showing pores, *i.e.*, cavitation, at a grain boundary. (For interpretation of the references to color in this figure legend, the reader is referred to the web version of this article.)

sliding was activated due to slip activity in adjacent grains. For the 90 ° configuration, grain boundary sliding was found to occur regardless of the development of plasticity in adjacent grains.

Concerning the influence of the grain misorientation, *i.e.*, the crystallographic configuration, on the onset and intensity of grain boundary sliding, high angle grain boundaries (HAGB) are particularly prone to strain localization at grain boundaries at room temperature (Fig. 14(a)) with misorientation leading to maximal strain intensity around 42 ± 8 °. Lower angle grain boundary (LAGB) can also activate strain localization but to a smaller extent in terms of strain intensity. At 350 °C, similar observations are found, but misorientation angles showing the most intense slip activity are in a broader range. This tendency with the temperature increase is also observed at 650 °C. HAGB is not a necessary condition for grain boundary sliding regardless of the investigated temperature, but most intense strain localization events are observed for misorientation angles between 20° and 50°.

4. Discussion

4.1. Temperature dependence of deformation mechanisms

In the present study, interrupted tensile tests paired with high-resolution digital image correlation were conducted from room temperature up to 650 °C on a polycrystalline Ni-based superalloy: the Alloy 718. The material experienced different deformation mechanisms at the microstructure scale as a function of the temperature. Intragranular slip, slip parallel to and near twin boundaries, and grain boundary sliding are not present in the same proportion and do not contribute similarly to the overall deformation depending on the temperature but also on the macroscopic plastic strain.

At room temperature, the micromechanical response of Ni-based superalloys has been widely investigated using HR-DIC [16,18,20,23,28,29,50–52]. The classification of the slip localization events with regard

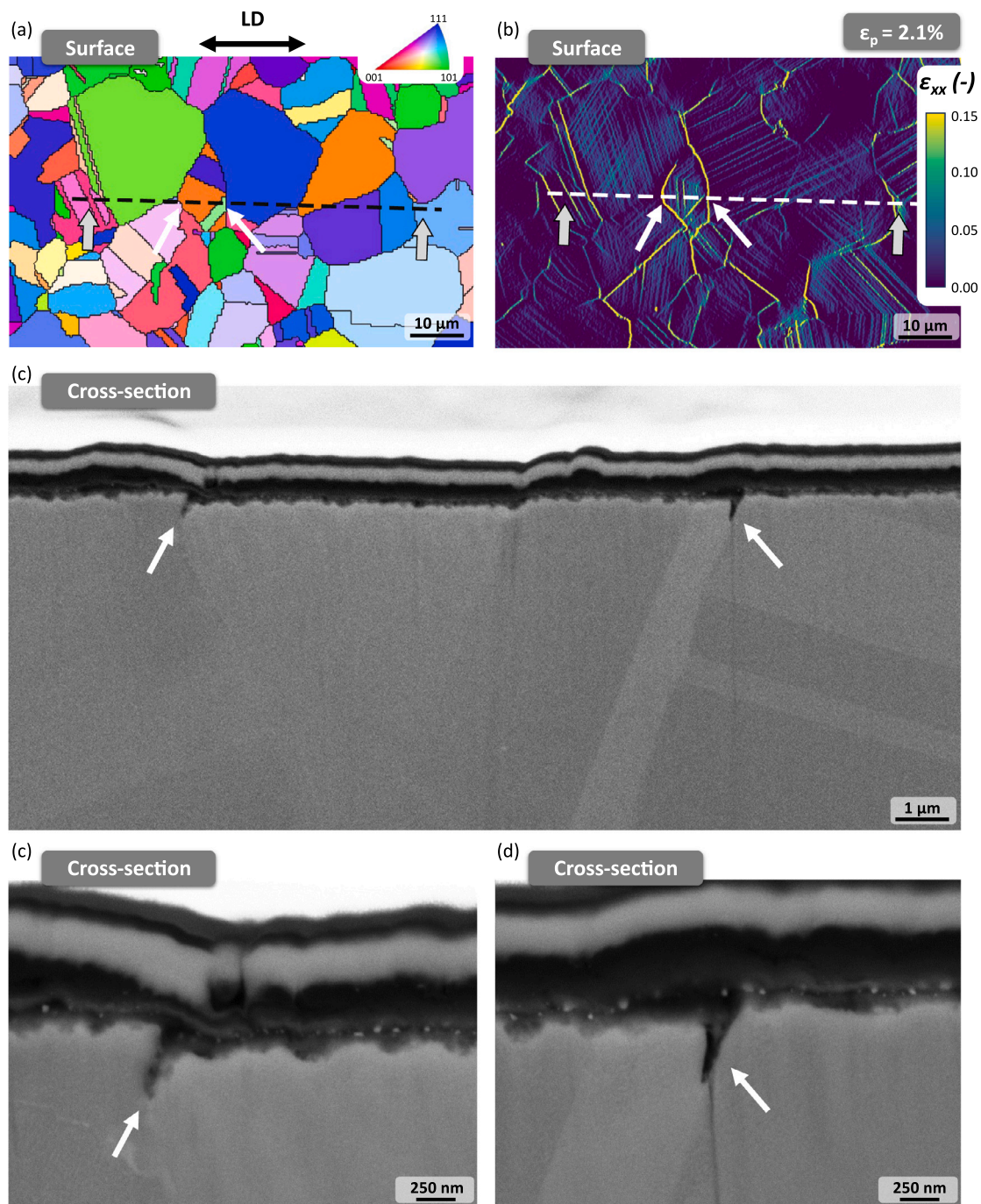


Fig. 11. Sub-surface damage development at 650 °C and 2.1 % plastic strain: grain boundary cracking at the external surface. (a) EBSD map of the specimen surface. The dashed line corresponds to the FIB cross-section. Gray arrows correspond to the cross-section observation direction. The white arrows highlight the location of grain boundaries of interest. (b) Strain map along the macroscopic loading direction. (c) EBSD map on the cross-section represented as IPF along the loading direction. (d) Kernel average misorientation (KAM) map. (e), (f), and (g) SEM images showing no cavitation but surface grain boundary cracking. (For interpretation of the references to color in this figure legend, the reader is referred to the web version of this article.)

to microstructural features has been reported in the literature for a similar Alloy 718 from surface observations [23] but also from volume characterizations using laser-based destructive 3D reconstruction techniques [28]. The present results agree well with the existing literature in terms of slip events classification as a function of the deformation level and the strain partition. Intense strain localization in the vicinity of twin boundaries is observed at the onset of plasticity but also at higher deformation levels (Figs. 12 and 13). This elementary deformation mechanism has been largely investigated by Stinville et al. [27,30,

53] and can find an explanation both in a large difference in elastic response between the twin and parent grain and a relatively high Schmid factor. Such microplasticity was demonstrated to be deleterious in terms of damage development under cyclic stresses up to intermediate temperature [27,53,54]. Furthermore, high density of intragranular slip events are intensively developing above the macroscopic yielding [23] and studied in previous HR-DIC studies [16,18,20,23,28,29,50–52]. The “highest” Schmid factor criterion is in average respected to describe intragranular slip activity for Ni-based superalloys. Despite the high propensity of intragranular slip events compared to slip parallel

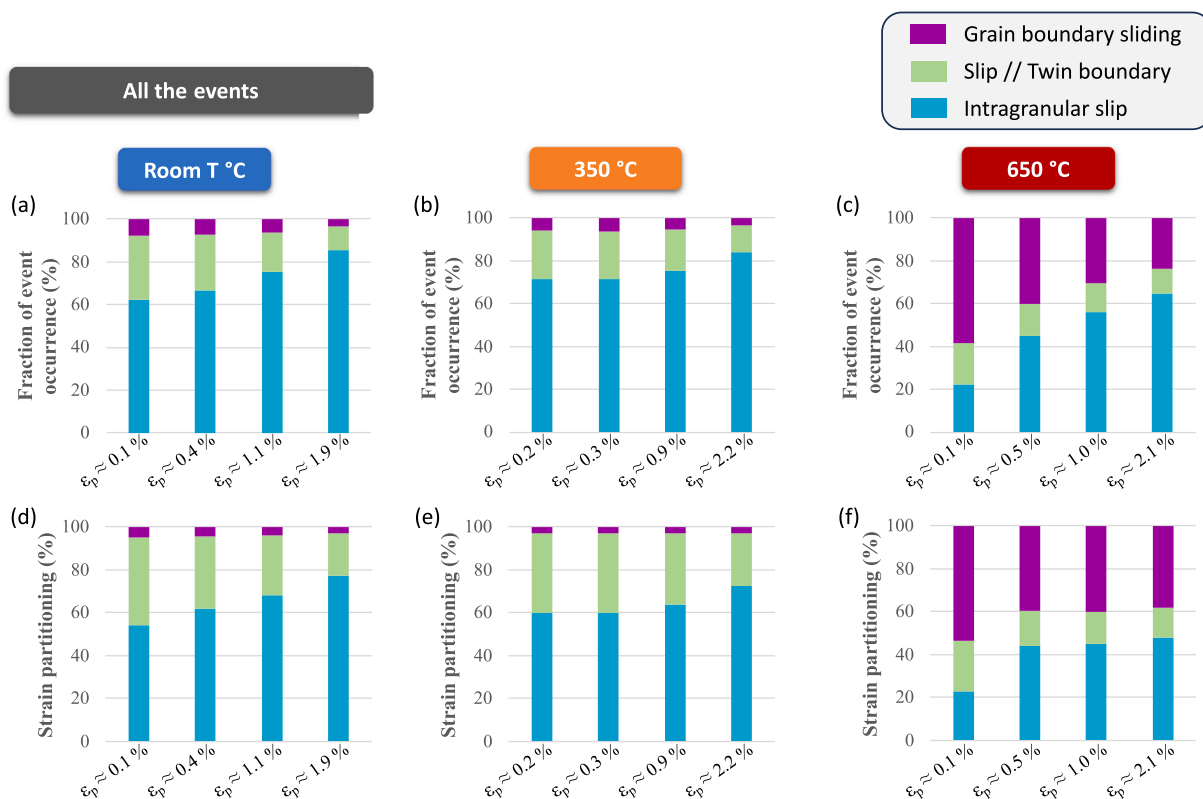


Fig. 12. Classification of strain localization and strain partitioning at the microstructure scale for different deformation levels and temperatures for all the strain localization events. Fraction of event occurrence as a function of the macroscopic plastic strain at (a) RT, (b) 350 °C, and (c) 650 °C. Strain partitioning as a function of the macroscopic plastic strain at (d) RT, (e) 350 °C, and (f) 650 °C. (For interpretation of the references to color in this figure legend, the reader is referred to the web version of this article.)

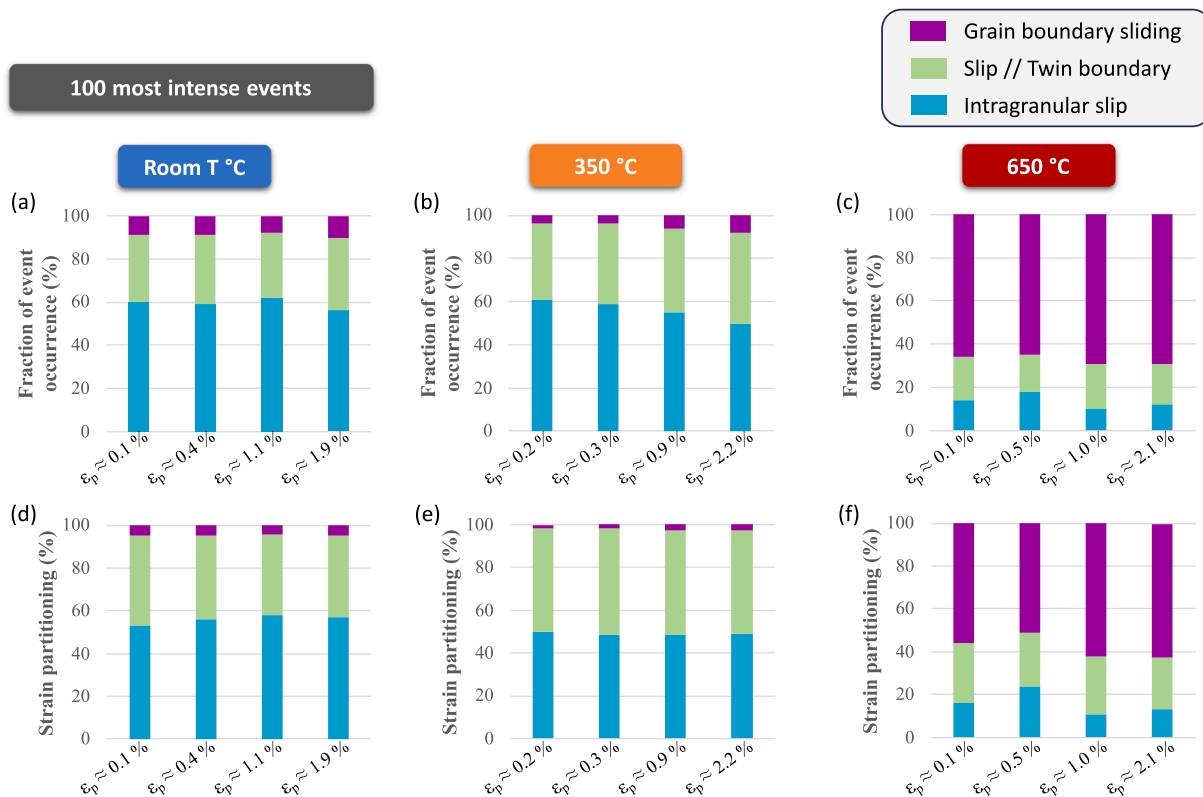


Fig. 13. Classification of strain localization and strain partitioning at the microstructure scale for different deformation levels and temperatures for the 100 most intense strain localization events. Fraction of event occurrence as a function of the macroscopic plastic strain at (a) RT, (b) 350 °C, and (c) 650 °C. Strain partitioning as a function of the macroscopic plastic strain at (d) RT, (e) 350 °C, and (f) 650 °C. (For interpretation of the references to color in this figure legend, the reader is referred to the web version of this article.)

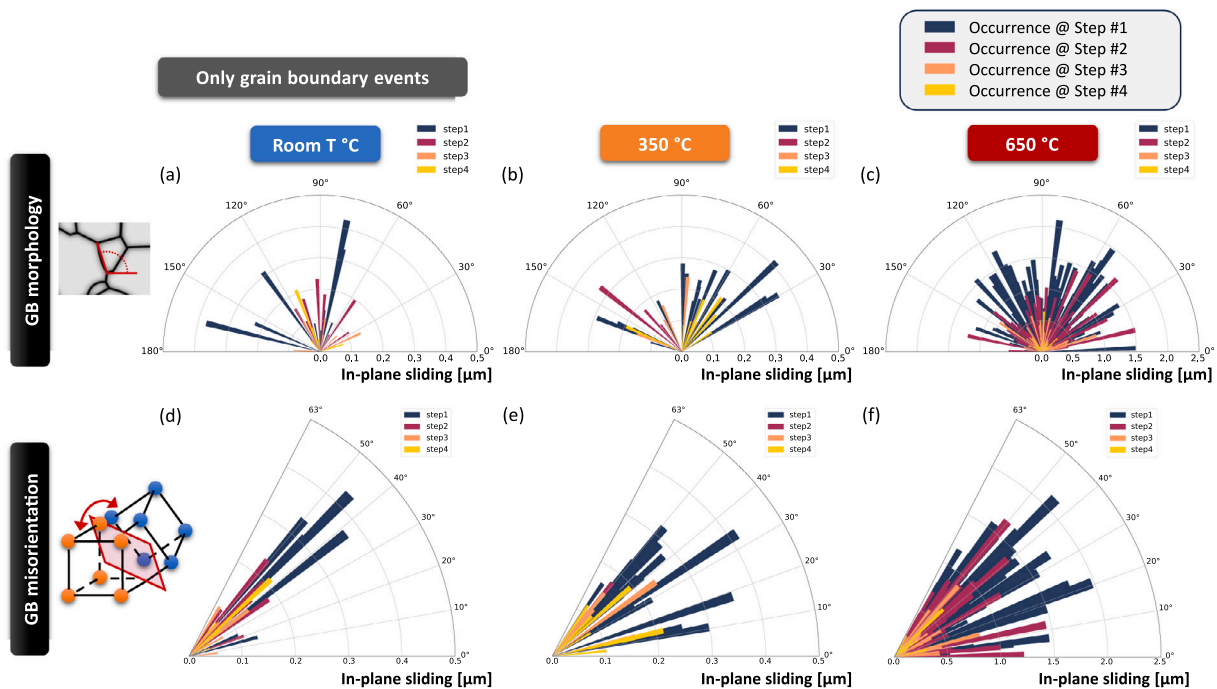


Fig. 14. Influence of the grain boundary morphological orientation on the onset and intensity of grain boundary sliding at (a) RT, (b) 350 °C, (c) 650 °C. Influence of the grain misorientation, *i.e.*, the crystallographic configuration, on the onset and intensity of grain boundary sliding at (a) RT, (b) 350 °C, (c) 650 °C. (For interpretation of the references to color in this figure legend, the reader is referred to the web version of this article.)

to and near twin boundaries, this latter elementary mechanism contributes to a high fraction of the overall deformation (Fig. 13). As grain boundary sliding/strain accumulation at grain boundaries is concerned, slip localization at twin boundaries was found to participate in the activation of microplasticity at grain boundaries at the onset of the plastic deformation. Higher deformation levels favor the occurrence of slip-stimulated grain boundary sliding, as reported in the literature [29]. Mechanisms at 350 °C were found similar despite the presence of PLC events during tensile testing, leading to jerky flow on the macroscopic stress–strain curve but also intense deformation bands at the mesoscale related to stress drop events. Strain partitioning at the microstructure scale inside and outside a PLC band is of high interest but was not considered here based on the small region of interest for HR-DIC. Mello et al. performed fatigue experiments paired with HR-DIC at 300 °C on a polycrystalline Ni-based superalloy (RR1000). Using slip trace analysis on strain field maps, they evidenced that the octahedral slip activity is solely represented at this temperature [40], as found in the present paper. Zhao et al. [52] found similar deformation mechanisms at 450 °C on an LSHR powder metallurgy alloy under fatigue testing using SEM-DIC and electron channeling contrast imaging (ECCI).

At 650 °C, microplasticity was found different for Alloy 718, grain boundary sliding being particularly intense regardless of the macroscopic deformation level. Grain boundary sliding occurred without the mediation of slip activity in adjacent grains, demonstrating the different nature of this elementary mechanism compared to slip-stimulated grain boundary sliding. Based on the cavitation process and rounded morphology of the pores, this deformation mechanism at grain boundaries seems to be a diffusion creep phenomenon, also denoted “Coble creep” in the literature [55]. While the kinematics order is different, the deformation mechanism at grain boundaries, assisted/enhanced or not by slip activity in adjacent grains, can be similar in nature. Grain boundary sliding is thus thermally activated, considering the concentration gradient of vacancies participating in the diffusion process along grain boundaries. Vacancy participation is also confirmed by the presence of pores at grain boundaries (see *e.g.* Figs. 9 and 10). This aspect will be further discussed in the section dedicated to grain boundary sliding and cavitation. Additional characterization

are yet necessary to clearly attribute such grain boundary sliding as Coble creep mechanisms. Dislocation glide can also be considered or also participate. Strain accumulation at grain boundaries and grain boundary sliding was also found for other Ni-based superalloys up to 850 °C using micro-grids techniques [10,11,32,39,56]. The spatial resolution of the microgrid [39,56] or microgrid plus sparsely distributed dots [10,11,32] was not sufficient to differentiate strain accumulation at grain boundaries from grain boundary sliding on strain maps. However, discrete shearing of microgrid clearly evidenced grain boundary sliding of superalloy at high temperature. Grain boundary sliding was observed more pronounced compared to intragranular slip under creep testing due to diffusive consideration under a steady loading condition, thus favoring the visco-plastic deformation at the microstructure scale [36,39]. In addition, Mello et al. evidenced the development of cubic slip activity in addition to the octahedral slip activity when increasing temperature up to 700 °C [40]. The authors reported the occurrence of cubic slip events for 1 % macroscopic strain at 550 °C and at lower deformation levels at 700 °C. However, they did not observe evidence of grain boundary sliding in this temperature range. This observation can be explained by the phase constitution of the studied material, *i.e.*, the RR1000 with γ' strengthening precipitates and the Alloy 718 with γ'' - γ' strengthening precipitates. γ'' , being less stable at 650 °C compared to the γ' phase, can be subject to diffusion processes favoring diffusion creep mechanisms and subsequently, grain boundary sliding. Stinville et al. also reported octahedral slip activity at 650 °C on a René88DT γ' -strengthened Ni-based superalloy without the occurrence of cubic slip systems and grain boundary sliding up to 1 % plastic strain [34]. These findings support improved mechanical properties at high temperature of γ' strengthening precipitates compared to γ'' strengthening precipitates Ni-based superalloys above 650 °C. However, they yet evidenced the importance of slip localization parallel to and near twin boundaries at 650 °C, leading to early oxidation-assisted cracking at twin boundaries under cyclic testing. In the present study, intense slip localization was also found at twin boundaries and only octahedral slip activity based on statistical slip trace and slip system analyses using H-DIC information merged with EBSD maps. Slip parallel to and near twin boundaries was found particularly intense

and interacted with grain boundaries leading to early grain boundary cracking/opening (Fig. 8). EBSD analyses in the sub-surface also evidenced a high degree of micro-rotations in grains adjacent to slip activity near a twin boundary demonstrating the particular role of twin boundaries in terms of microplasticity (Fig. 9). Intragranular slip was generally not intense enough to induce such plasticity transfer in adjacent grains. Carter et al. also reported a particularly intense strain localization/accumulation at high temperatures on a Rene-104 Ni-based superalloy [32]. They evidenced very little intragranular strain accumulation at high temperatures, and annealing twin boundaries played an important role in strain localization sites. However, they also demonstrated the role of grain boundary structure using SEM-DIC techniques on serrated grain boundary structure, showing a lower contribution of grain boundary sliding to the overall strain accommodation. Therefore, the three-dimensional grain morphology and grain size play a key role in the grain boundary sliding intensity. Further three-dimensional characterizations similar to Charpagne et al. using Tribem techniques [28] or Ludwig and Proudhon et al. using diffraction contrast tomography (DCT) and topotomography [53] would be beneficial to identify the grain morphology as well as crystal lattice rotation thanks to diffraction techniques.

4.2. Cavitation associated with grain boundary sliding/cracking

Grain boundary sliding was evidenced at 650 °C for Alloy 718 using HR-DIC (Fig. 6). While oxidation-assisted intergranular cracking has been widely investigated for the Alloy 718 due to potential oxygen diffusion and/or vacancy injection at grain boundaries under air and dynamic diffusion/deformation processes [57–60], intergranular cracking of Alloy 718 still remains valid under vacuum for low strain rate conditions. Different damage mechanisms at grain boundaries were found (i) faceted cracks at grain boundaries (Figs. 7 and 8) and (ii) voided-grain boundary sliding (Figs. 9 and 10). Voided-grain boundary sliding, *i.e.*, cavitation, was only observed for two examples and required more sub-surface observations to confirm the representativeness of the event.

For faceted cracks at grain boundaries, grain boundary sliding can be at the origin of such granular fractures due to intense strain localization events at grain boundaries, even in the absence of slip activity in adjacent grains. However, larger deformation levels impose intragranular slip to populate grains, leading to additional strain accumulation at grain boundaries due to single slip/multiple slip events. Stinville et al. [61] investigated creep-deformation in a DS200 superalloy using mesoscale DIC and reported that intergranular cracks form at high angle grain boundaries separating grains with a relatively low rotation (*e.g.* (001) oriented grains) and a grain favorably oriented for single slip activity with a relatively high Schmid factor. HAGB was found to be a condition favoring grain boundary sliding, especially at early deformation levels (Fig. 14). In addition, grain morphology at the surface and also in the volume play a significant role in the sliding activity, as well as the displacement jump direction in regard to the grain boundary orientation. Inclined grain boundaries in reference to the loading direction might favor mode II grain boundary sliding. However, this surface and subsurface morphological consideration is not sufficient to fully dissociate grain boundary sliding, that is a mode II-dominated deformation process, compared to grain opening, that is a mode I-dominated deformation process. Therefore, three-dimensional kinematics are necessary to state on these deformation modes since out-of-plane height steps at the surface would be informative of grain boundary sliding. In addition, local stress concentration in the vicinity of triple junctions, in combination with other grain boundary deformation, might lead to local grain boundary weakening, cavitation and then cracking. In addition, intense slip activity parallel to and near twin boundaries was also found to interact and weaken adjacent grain boundaries at their extremities, leading to particular grain boundary opening/cracking (Fig. 8). Such microstructural configurations are present due to annealing twins in the material.

For voided-grain boundary sliding, vacancy aggregation under the influence of stress and vacancy supersaturation could induce void growth at grain boundary under diffusive creep [55,62–67]. Vacancies are maintained near equilibrium as a result of applied stress, leading to void formation at grain boundaries. Even if such damage mechanisms are generally reported for creep testing, tensile tests were performed at a relatively low strain rate, enabling viscoplastic contribution at the microscale during monotonic loading. Additional details on both the nucleation and growth of voids at grain boundaries, in the presence or not of slip activity, are well described in Ref. [67]. In the present study, voids are present at grain boundaries at hundreds of nanometers beneath the external surface but not in the bulk material. The surface is a particular boundary condition due to deformation capabilities in the presence of a “free-surface” but also due to potential surface reactivity. Larger deformation can occur at a free-surface due to dislocation escape and surface roughening capabilities that neighboring grains cannot offer (grain confinement in the volume). Even if high vacuum limits oxidation, chromia-forming alloys are still reactive at 650 °C, and dynamic embrittlement remains possible due to vacancy injection under cationic oxidation mechanisms. The color of the specimens slightly changed after each deformation step but resulted in an increase of 20 to 50 nm of the external oxide scale owing to the change in color. Therefore, cavitation near the surface and not in the volume can also originate from the slight oxidation, greater for interrupted tests compared to monotonic tests due to transient heating phases leading to increased thermal exposure. In addition, void formation can also result from cooling for SEM observation, leading to potential vacancy condensation. Such intense microplasticity can thus interact with grain boundary and lead to slip-induced void nucleation or grain boundary sliding. In the present study, morphological as well as crystallographic considerations aimed at describing parameters leading to grain boundary cavitation. Kinematics fields at the specimen surface aimed at highlighting that displacement jump related to grain boundary sliding nearly normal to the grain boundary trace (mode I stress condition) at the surface favors sub-surface grain cavitation if the grain boundary is nearly vertical in the volume and has a misorientation angle higher than 20°. Van der Giessen et al. [66] numerically investigated grain boundary cavitation and sliding at grain facets normal, inclined, and transverse to the maximum principal tensile stress and found the importance of orthogonal grain boundaries to the maximum principal loading direction to form cavitation and micro-crack.

4.3. Crystallographic slip and morphological sliding: a necessity to assess 3D kinematics field at the microscale

Previous discussions on microplasticity and damage development at the microstructure scale were done using in-plane strain field measurements. However, assessment of the out-of-plane component is of prime importance at elevated temperature due to the morphological sliding or opening of grain boundaries under stresses. In the present investigation, only post-mortem topographic analyses were performed using laser scanning confocal microscopy for informative and qualitative observations, as illustrated in **supplementary material**. The quality of the surface preparation prior to deformation was not enough to combine height step for each strain localization events for statistical 3D characterization of the microplasticity. The 3D kinematics field at the microscale will be further investigated in future work considering the initial topography of the sample, similarly to Ref. [23].

At room temperature and 350 °C, octahedral slip activity was mostly distributed intragranularly, and parallel to and near twin boundaries. Such slip activity is crystallographic and can be identified using in-plane kinematics fields to measure the cumulated Burgers vector projected onto the observation surface and EBSD measurements. In-plane deformation analysis may be sufficient for crystallographic slip. Still, localized slip mechanisms can be complex, and three-dimensional analysis of these surface displacement discontinuities is essential to quantify

the actual slip amplitude due to the activation and interaction of several active systems or morphological slip (slip at grain boundaries, interfaces, interphases, etc.). Necessity of three-dimensional measurements was demonstrated by Liu et al. for multiple slip activity in the same slipping plane parallel to and near a twin boundary [23]. Although the resolution and spatial repeatability of optical observation methods are inferior to those of scanning electron microscopy, laser scanning confocal microscopy (LSCM) at short wavelengths offers a decisive advantage in the three-dimensional identification of local relative displacements of a few tens of nanometers [23,24]. For smaller displacements, atomic force microscopy remains the most effective tool but is limited in the region to be investigated [29,68–74]. Such out-of-plane component identifications are essential for three-dimensional deformation that cannot be easily estimated from in-plane measurement, such as morphological sliding related to grain boundary sliding. For grain boundary sliding and damage development, topographic measurements in conjunction with three-dimensional subsurface microstructure knowledge are most crucial. This measurement of three-dimensional kinematics at high temperature will be the subject of further examination using either combinational SEM plus LSCM imaging or solely LSCM.

5. Conclusions

High-resolution digital image correlation (HR-DIC) measurements were conducted on an Alloy 718 from room temperature up to 650 °C to document strain localization development in the early plastic deformation domain at the microstructure scale. Data registration and merging techniques using EBSD information and kinematics fields aimed at identifying and classifying strain localization events as a function of the interaction with the microstructural features, *i.e.*, intragranular slip, slip localization parallel to and near twin boundaries and grain boundary sliding. While Alloy 718 has been intensively investigated at room temperature, the deformation and early damage mechanisms identified and their statistical analysis at intermediate and high temperatures constitute the originality of the present work. It aimed to inform on the intergranular fracture occurring at high temperature and relatively low strain rates for this material. Alloy 718 experienced similar microplasticity at room temperature and 350 °C, strain partitioning being mainly distributed near twin boundaries and intragranularly. Grain boundary sliding up to intermediate temperature is relatively insignificant but increases due to the apparition of slip-stimulated grain boundary sliding above 1 % plastic strain. At 650 °C, strain localization at grain boundaries is particularly intense and not necessarily assisted by slip in adjacent grains. Different damage mechanisms were identified: (i) grain boundary cracking/opening due to intense slip activity at an adjacent twin boundary, (ii) diffusive cavitation at grain boundaries, (iii) grain boundary cracking. Kinematics fields and cross-sectional information on the microstructure helped to identify deformation modes favoring the occurrence of cavitation at grain boundaries, *i.e.*, orthogonal grain boundary relative to the loading direction, a sliding direction nearly perpendicular to the grain boundary trace at the surface, a relatively high grain misorientation. Laser scanning confocal microscopy (LSCM) aimed to evaluate the out-of-plane deformation component, particularly necessary for evaluating grain boundary sliding due to its morphological sliding character.

6. License

This research was funded, in part, by The European Research Council, project HT-S₄DefOx - Grant number 948007. A [CC-BY public copyright license] has been applied by the authors to the present document and will be applied to all subsequent versions up to the Author Accepted Manuscript arising from this submission, in accordance with the grant's open access conditions.

Declaration of competing interest

The authors declare the following financial interests/personal relationships which may be considered as potential competing interests: Damien TEXIER reports financial support was provided by European Research Council. Jean-Charles Stinville reports financial support was provided by National Science Foundation. Damien TEXIER reports financial support was provided by Centre National de la Recherche Scientifique. If there are other authors, they declare that they have no known competing financial interests or personal relationships that could have appeared to influence the work reported in this paper.

Data availability

The raw/processed data required to reproduce these findings cannot be shared at this time as the data also forms part of an ongoing study.

Acknowledgments

This work was supported by the European Research Council [project HT-S₄DefOx - Grant number 948007]. The authors are grateful to the *Centre National de la Recherche Scientifique (CNRS)* for the mobility grant with the International Research Project denoted "CIN&MAT". JCS acknowledges the National Science Foundation (award #2234892) for financial support. The authors thank B. Gueraud and Y. Vidalenc for cross-sectional characterizations and V. Valle for Heaviside-DIC developments. The authors particularly acknowledge the Raimond Castaing Microanalysis Centre (UAR 3623) for access to scanning electron microscopy access and microprobe analyses.

Appendix A. Supplementary data

Supplementary material related to this article can be found online at <https://doi.org/10.1016/j.actamat.2024.119759>.

References

- [1] V. Garat, J.M. Cloue, D. Poquillon, E. Andrieu, Influence of Portevin-Le Chatelier effect on rupture mode of alloy 718 specimens, *J. Nucl. Mater.* 375 (1) (2008) 95–101, <http://dx.doi.org/10.1016/j.jnucmat.2007.10.009>.
- [2] B. Max, B. Viguier, E. Andrieu, J. Cloue, A re-examination of the Portevin-Le Chatelier effect in Alloy 718 in connection with oxidation-assisted intergranular cracking, *Metall. Mater. Trans. A* 45 (12) (2014) 5431–5441, <http://dx.doi.org/10.1007/s11661-014-2508-6>.
- [3] E. Andrieu, B. Max, B. Viguier, Oxidation assisted intergranular cracking in Alloy 718: Effects of strain rate and temperature, *AerospaceLab Journal* 9 (2015) 1–7, <http://dx.doi.org/10.12762/2015.AL09-09>.
- [4] Z. Zhao, M. Ramesh, D. Raabe, A. Cuitiño, R. Radovitzky, Investigation of three-dimensional aspects of grain-scale plastic surface deformation of an aluminum oligocrystal, *Int. J. Plast.* 24 (12) (2008) 2278–2297, <http://dx.doi.org/10.1016/j.jiplas.2008.01.002>.
- [5] J. Carroll, W. Abuzaid, J. Lambros, H. Sehitoglu, An experimental methodology to relate local strain to microstructural texture, *Rev. Sci. Instrum.* 81 (8) (2010) <http://dx.doi.org/10.1063/1.3474902>.
- [6] W.Z. Abuzaid, M.D. Sangid, J.D. Carroll, H. Sehitoglu, J. Lambros, Slip transfer and plastic strain accumulation across grain boundaries in Hastelloy X, *J. Mech. Phys. Solids* 60 (6) (2012) 1201–1220, <http://dx.doi.org/10.1016/j.jmps.2012.02.001>.
- [7] P. Doumalin, M. Bornert, Micromechanical applications of digital image correlation techniques, in: P. Jacquot, J.-M. Fournier (Eds.), *Interferometry in Speckle Light*, 2000, pp. 67–74, http://dx.doi.org/10.1007/978-3-642-57323-1_9.
- [8] F. Lagattu, F. Bridier, P. Villechaise, J. Brillaud, In-plane strain measurements on a microscopic scale by coupling digital image correlation and an in situ SEM technique, *Mater. Charact.* 56 (1) (2006) 10–18, <http://dx.doi.org/10.1016/j.matchar.2005.08.004>.
- [9] M. Sutton, N. Li, D. Garcia, N. Cornille, J. Orteu, S. McNeill, H. Schreier, X. Li, A. Reynolds, Scanning electron microscopy for quantitative small and large deformation measurements Part II: Experimental validation for magnifications from 200 to 10,000, *Exp. Mech.* 47 (2007) 789–804, <http://dx.doi.org/10.1007/s11340-007-9041-0>.
- [10] J. Walley, R. Wheeler, M. Uchic, M. Mills, In-Situ mechanical testing for characterizing strain localization during deformation at elevated temperatures, *Exp. Mech.* 52 (2012) 405–416, <http://dx.doi.org/10.1007/s11340-011-9499-7>.

- [11] J. Carter, N. Zhou, J. Sosa, P. Shade, A. Pilchak, M. Kuper, Y. Wang, H. Fraser, M. Uchic, M. Mills, Characterization of strain accumulation at grain boundaries of nickel-based superalloys, in: E. Huron, R. Reed, M. Hardy, M. Mills, R. Montero, P. Portella, J. Telesman (Eds.), *Superalloys 2012*, Champion, PA (USA), 2012, pp. 43–52.
- [12] F. Bridier, J.-C. Stinville, N. Vanderesse, P. Villechaise, P. Bocher, Microscopic strain and crystal rotation measurement within metallurgical grains, *Key Eng. Mater.* (2013) 592–593, <http://dx.doi.org/10.4028/www.scientific.net/kem.592-593.493>.
- [13] N. Vanderesse, M. Lagacé, F. Bridier, P. Bocher, An open source software for the measurement of deformation fields by means of digital image correlation, *Microsc. Microanal.* 19 (S2) (2013) 820–821, <http://dx.doi.org/10.1017/S1431927613006090>.
- [14] F. Di Gioacchino, J. Quinta da Fonseca, Plastic strain mapping with sub-micron resolution using digital image correlation, *Exp. Mech.* 53 (5) (2013) 743–754, <http://dx.doi.org/10.1007/s11340-012-9685-2>.
- [15] A.D. Kammers, S. Daly, Digital image correlation under scanning electron microscopy: Methodology and validation, *Exp. Mech.* 53 (9) (2013) 1743–1761, <http://dx.doi.org/10.1007/s11340-013-9782-x>.
- [16] J. Stinville, M. Echlin, D. Texier, F. Bridier, P. Bocher, T. Pollock, Sub-grain scale digital image correlation by electron microscopy for polycrystalline materials during elastic and plastic deformation, *Exp. Mech.* 56 (2016) 197–216, <http://dx.doi.org/10.1007/s11340-015-0083-4>.
- [17] T.E.J. Edwards, F. Di Gioacchino, R. Muñoz-Moreno, W.J. Clegg, Deformation of lamellar TiAl alloys by longitudinal twinning, *Scr. Mater.* 118 (2016) 46–50, <http://dx.doi.org/10.1016/j.scriptamat.2016.03.004>.
- [18] R. Jiang, F. Pierron, S. Octaviani, P. Reed, Characterisation of strain localisation processes during fatigue crack initiation and early crack propagation by SEM-DIC in an advanced disc alloy, *Mater. Sci. Eng. A* 699 (2017) 128–144, <http://dx.doi.org/10.1016/j.msea.2017.05.091>.
- [19] Y. Guan, B. Chen, J. Zou, T.B. Britton, J. Jiang, F.P. Dunne, Crystal plasticity modelling and HR-DIC measurement of slip activation and strain localization in single and oligo-crystal Ni alloys under fatigue, *Int. J. Plast.* 88 (2017) 70–88, <http://dx.doi.org/10.1016/j.ijplas.2016.10.001>.
- [20] F. Bourdin, J.C. Stinville, M.P. Echlin, P.G. Callahan, W.C. Lenthe, C.J. Torbet, D. Texier, F. Bridier, J. Cormier, P. Villechaise, T.M. Pollock, V. Valle, Measurements of plastic localization by Heaviside-digital image correlation, *Acta Mater.* 157 (2018) 307–325, <http://dx.doi.org/10.1016/j.actamat.2018.07.013>.
- [21] X. Xu, D. Lunt, R. Thomas, R.P. Babu, A. Harte, M. Atkinson, J.Q. da Fonseca, M. Preuss, Identification of active slip mode in a hexagonal material by correlative scanning electron microscopy, *Acta Mater.* 175 (2019) 376–393, <http://dx.doi.org/10.1016/j.actamat.2019.06.024>.
- [22] M. Bertin, C. Du, J.P. Hoefnagels, F. Hild, Crystal plasticity parameter identification with 3D measurements and integrated digital image correlation, *Acta Mater.* 116 (2016) 321–331, <http://dx.doi.org/10.1016/j.actamat.2016.06.039>.
- [23] J. Liu, N. Vanderesse, J.-C. Stinville, T. Pollock, P. Bocher, D. Texier, In-plane and out-of-plane deformation at the sub-grain scale in polycrystalline materials assessed by confocal microscopy, *Acta Mater.* 169 (2019) 260–274, <http://dx.doi.org/10.1016/j.actamat.2019.03.001>.
- [24] W. Yin, F. Briffod, H. Hu, T. Shiraiwa, M. Enoki, Three-dimensional configuration of crystal plasticity in stainless steel assessed by high resolution digital image correlation and confocal microscopy, *Int. J. Plast.* 170 (2023) 103762, <http://dx.doi.org/10.1016/j.ijplas.2023.103762>.
- [25] Z. Chen, S. Daly, Active slip system identification in polycrystalline metals by Digital Image Correlation (DIC), *Exp. Mech.* 57 (2017) 115–127, <http://dx.doi.org/10.1007/s11340-016-0217-3>.
- [26] T. Vermeij, R. Peerlings, M. Geers, J. Hoefnagels, Automated identification of slip system activity fields from digital image correlation data, *Acta Mater.* 243 (2023) 118502, <http://dx.doi.org/10.1016/j.actamat.2022.118502>.
- [27] J. Stinville, N. Vanderesse, F. Bridier, P. Bocher, T. Pollock, High resolution mapping of strain localization near twin boundaries in a nickel-based superalloy, *Acta Mater.* 98 (2015) 29–42, <http://dx.doi.org/10.1016/j.actamat.2015.07.016>.
- [28] M. Charpagne, J. Hestroffer, A. Polonsky, M. Echlin, D. Texier, V. Valle, I. Beyerlein, T. Pollock, J. Stinville, Slip localization in Inconel 718: A three-dimensional and statistical perspective, *Acta Mater.* 215 (2021) 117037, <http://dx.doi.org/10.1016/j.actamat.2021.117037>.
- [29] R. Sperry, S. Han, Z. Chen, S.H. Daly, M.A. Crimp, D.T. Fullwood, Comparison of EBSD, DIC, AFM, and ECCI for active slip system identification in deformed Ti-7Al, *Mater. Charact.* 173 (2021) 110941, <http://dx.doi.org/10.1016/j.matchar.2021.110941>.
- [30] J. Stinville, W. Lenthe, J. Miao, T. Pollock, A combined grain scale elastic–plastic criterion for identification of fatigue crack initiation sites in a twin containing polycrystalline nickel-base superalloy, *Acta Mater.* 103 (2016) 461–473, <http://dx.doi.org/10.1016/j.actamat.2015.09.050>.
- [31] G. Martin, D. Caldemaison, M. Bornert, C. Pinna, Y. Bréchet, M. Véron, J.D. Mithieux, T. Pardoen, Characterization of the high temperature strain partitioning in duplex steels, *Exp. Mech.* 53 (2) (2013) 205–215, <http://dx.doi.org/10.1007/s11340-012-9628-y>.
- [32] J. Carter, M. Kuper, M. Uchic, M. Mills, Characterization of localized deformation near grain boundaries of superalloy René-104 at elevated temperature, *Mater. Sci. Eng. A* 605 (2014) 127–136, <http://dx.doi.org/10.1016/j.msea.2014.03.048>.
- [33] J. Carter, M. Uchic, M. Mills, Impact of speckle pattern parameters on DIC strain resolution calculated from in-situ SEM experiments, in: *Fracture, Fatigue, Failure, and Damage Evolution*, vol. 5, 2015, pp. 119–126, http://dx.doi.org/10.1007/978-3-319-06977-7_16.
- [34] J.C. Stinville, M.P. Echlin, P.G. Callahan, V.M. Miller, D. Texier, F. Bridier, P. Bocher, T.M. Pollock, Measurement of strain localization resulting from monotonic and cyclic loading at 650 °C in nickel base superalloys, *Exp. Mech.* 57 (8) (2017) 1289–1309, <http://dx.doi.org/10.1007/s11340-017-0286-y>.
- [35] T.E. Edwards, F. Di Gioacchino, H.P. Springbett, R.A. Oliver, W.J. Clegg, Stable speckle patterns for nano-scale strain mapping up to 700 °C, *Exp. Mech.* 57 (9) (2017) 1469–1482, <http://dx.doi.org/10.1007/s11340-017-0317-8>.
- [36] F. Bourdin, *Analyse Des Processus D'endommagement Aux Joints De Grains Dans Les Superalloys Base Nickel* (Ph.D. thesis), ISAE-ENSMA, Poitiers, 2020.
- [37] T.E.J. Edwards, F. Di Gioacchino, W.J. Clegg, High resolution digital image correlation mapping of strain localization upon room and high temperature, high cycle fatigue of a TiAl intermetallic alloy, *Int. J. Fatigue* 142 (2021) 105905, <http://dx.doi.org/10.1016/j.ijfatigue.2020.105905>.
- [38] M.F. Kiu, C. Pinna, D.C. Farrugia, New experimental procedure for the analysis of micro-Scale surface damage at high temperature, *Exp. Mech.* 56 (6) (2016) 1063–1072, <http://dx.doi.org/10.1007/s11340-016-0151-4>.
- [39] A. Soula, D. Locq, D. Boivin, Y. Renollet, P. Caron, Y. Bréchet, Quantitative evaluation of high temperature deformation mechanisms: A specific microgrid extensometry technique coupled with EBSD analysis, *J. Mater. Sci.* 45 (2010) 5649–5659, <http://dx.doi.org/10.1007/s10853-010-4630-1>.
- [40] A.W. Mello, A. Nicolas, M.D. Sangid, Fatigue strain mapping via digital image correlation for Ni-based superalloys: The role of thermal activation on cube slip, *Mater. Sci. Eng. A* 695 (April) (2017) 332–341, <http://dx.doi.org/10.1016/j.msea.2017.04.002>.
- [41] R. Bigger, B. Blaysat, C. Boo, M. Grever, J. Hu, A. Jones, M. Klein, P. Lava, M. Pankow, K. Raghavan, P.L. Reu, T. Schmidt, T. Siebert, M. Simonsen, A. Trim, D.Z. Turner, A. Vieira, T. Weikert, A good practices guide for digital image correlation, 2018, URL <https://api.semanticscholar.org/CorpusID:69964021>.
- [42] T. Kroeger, R. Timofte, D. Dai, L.V. Gool, Fast optical flow using dense inverse search, in: *Proceedings of the European Conference on Computer Vision, ECCV, 2016*, <http://dx.doi.org/10.48550/arXiv.1603.03590>.
- [43] P. Weinzapfel, J. Revaud, Z. Harchaoui, C. Schmid, DeepFlow: Large displacement optical flow with deep matching, in: *ICCV 2013 - IEEE International Conference on Computer Vision, 2013*.
- [44] V. Valle, S. Hedan, P. Cosenza, A.L. Fauchille, M. Berdjane, Digital image correlation development for the study of materials including multiple crossing cracks, *Exp. Mech.* 55 (2) (2015) 379–391, <http://dx.doi.org/10.1007/s11340-014-9948-1>.
- [45] M. Charpagne, J. Stinville, P. Callahan, D. Texier, Z. Chen, P. Villechaise, V. Valle, T. Pollock, Automated and quantitative analysis of plastic strain localization via multi-modal data recombination, *Mater. Charact.* 163 (2020) 110245, <http://dx.doi.org/10.1016/j.matchar.2020.110245>.
- [46] A. Rouwane, D. Texier, S. Hémy, J.-C. Passieux, Q. Sirvin, J. Gené, A. Proietti, J.-C. Stinville, Strain localization in Ti and Ti-allys using three-dimensional topographic imaging, in: *Titanium 2023*, 2023.
- [47] S. Hémy, C. Trosas, P. Villechaise, Slip-stimulated grain boundary sliding in Ti-6Al-4V at room temperature, *Materialia* 5 (2019) <http://dx.doi.org/10.1016/j.mtla.2018.100189>.
- [48] P. Villechaise, J. Cormier, T. Billot, J. Mendez, Mechanical behavior and damage processes of Udimet 720Li: Influence of localized plasticity at grain boundaries, in: *Superalloys 2012*, Champion, PA (USA), 2012, pp. 13–24, <http://dx.doi.org/10.1002/9781118516430.ch2>.
- [49] B. Larrouy, P. Villechaise, J. Cormier, O. Berteaux, Grain boundary-slip bands interactions: Impact on the fatigue crack initiation in a polycrystalline forged Ni-based superalloy, *Acta Mater.* 99 (2015) 325–336, <http://dx.doi.org/10.1016/j.actamat.2015.08.009>.
- [50] J. Stinville, W. Lenthe, M. Echlin, P. Callahan, D. Texier, T. Pollock, Microstructural statistics for fatigue crack initiation in polycrystalline nickel-base superalloys, *Int. J. Fract.* 208 (2017) 221–240, <http://dx.doi.org/10.1007/s10704-017-0241-z>.
- [51] J. Stinville, M. Charpagne, F. Bourdin, P. Callahan, Z. Chen, M. Echlin, D. Texier, J. Cormier, P. Villechaise, T. Pollock, V. Valle, Measurement of elastic and rotation fields during irreversible deformation using Heaviside-digital image correlation, *Mater. Charact.* 169 (April) (2020) 110600, <http://dx.doi.org/10.1016/j.matchar.2020.110600>.
- [52] Y. Zhao, R. Jiang, A. Harte, D.J. Bull, P.A. Reed, Characterisation of strain localisation under cyclic loading at 450 °C by SEM-DIC in a PM Ni-based superalloy, *Mater. Sci. Eng. A* 849 (2022) 143464, <http://dx.doi.org/10.1016/j.msea.2022.143464>.
- [53] J. Stinville, W. Ludwig, P.G. Callahan, M.P. Echlin, V. Valle, T.M. Pollock, H. Proudhon, Observation of bulk plasticity in a polycrystalline titanium alloy by diffraction contrast tomography and topotomography, *Mater. Charact.* 188 (November 2021) (2022) 111891, <http://dx.doi.org/10.1016/j.matchar.2022.111891>.

- [54] J.-C. Stinville, E. Martin, M. Karadge, S. Ismonov, M. Soare, T. Hanlon, S. Sundaram, M. Echlin, P. Callahan, W. Lenthe, J. Miao, A. Wessman, R. Finlay, A. Loghini, J. Marte, T. Pollock, Competing modes for crack initiation from non-metallic inclusions and intrinsic microstructural features during fatigue in a polycrystalline nickel-based superalloy, *Metall. Mater. Trans. A* (2018) <http://dx.doi.org/10.1007/s11661-018-4780-3>.
- [55] R. Coble, A model for boundary diffusion controlled creep in polycrystalline materials, *J. Appl. Phys.* 34 (6) (1963) 1679–1682, <http://dx.doi.org/10.1063/1.1702656>.
- [56] K. Thibault, D. Locq, P. Caron, D. Boivin, Y. Renollet, Y. Bréchet, Influence of microstructure on local intra- and intergranular deformations during creep of a nickel-based superalloy at 700°C, *Mater. Sci. Eng. A* 588 (2013) 14–21, <http://dx.doi.org/10.1016/j.msea.2013.09.015>.
- [57] E. Andrieu, R. Cozar, A. Pineau, Effect of environment and microstructure on the high temperature behavior of Alloy 718, in: *Superalloys 718 Metallurgy and Applications*, The Minerals, Metals & Materials Society, 1989, pp. 241–256, http://dx.doi.org/10.7449/1989/superalloys_1989_241_256.
- [58] E. Andrieu, R. Molins, H. Ghonem, A. Pineau, Intergranular crack tip oxidation mechanism in a nickel-based superalloy, *Mater. Sci. Eng. A* 154 (1992) 21–28, [http://dx.doi.org/10.1016/0921-5093\(92\)90358-8](http://dx.doi.org/10.1016/0921-5093(92)90358-8).
- [59] H. Ghonem, T. Nicholas, A. Pineau, Elevated temperature fatigue crack growth in Alloy 718—Part I: Effects of environmental and material variables, *Fatigue Fract. Eng. Mater. Struct.* 16 (6) (1993) 577–590, <http://dx.doi.org/10.1111/j.1460-2695.1993.tb00103.x>.
- [60] J.A. Pfandtner, J.J. McMahon, Oxygen-induced intergranular cracking of a Ni-base alloy at elevated temperatures - An example of dynamic embrittlement, *Acta Mater.* 49 (16) (2001) 3369–3377, [http://dx.doi.org/10.1016/S1359-6454\(01\)00005-2](http://dx.doi.org/10.1016/S1359-6454(01)00005-2).
- [61] J.C. Stinville, L. Mataveli Suave, F. Maugé, L. Marcin, P. Villechaise, T.M. Pollock, J. Cormier, Damage nucleation during transverse creep of a directionally solidified Ni-based superalloy, *Mater. Sci. Eng. A* 858 (2022) 144089, <http://dx.doi.org/10.1016/j.msea.2022.144089>.
- [62] R. Balluffi, L. Seigle, Growth of voids in metals during diffusion and creep, *Acta Metall.* 5 (8) (1957) 449–454, [http://dx.doi.org/10.1016/0001-6160\(57\)90063-9](http://dx.doi.org/10.1016/0001-6160(57)90063-9).
- [63] A. Perry, Cavitation in creep, *J. Mater. Sci.* 9 (6) (1974) 1016–1039, <http://dx.doi.org/10.1007/BF00570398>.
- [64] J. Hancock, Creep cavitation without a vacancy flux, *Metal Sci.* 10 (9) (1976) 319–325, <http://dx.doi.org/10.1179/msc.1976.10.9.319>.
- [65] A. Needleman, J. Rice, *Plastic Creep Flow Effects in the Diffusive Cavitation of Grain Boundaries*, Third Edit, Perspectives in Creep Fracture, vol. 28, (9) Pergamon Press Ltd, 1983, pp. 107–124, <http://dx.doi.org/10.1016/b978-0-08-030541-7.50009-6>.
- [66] E. van der Giessen, V. Tvergaard, A creep rupture model accounting for cavitation at sliding grain boundaries, *Int. J. Fract.* 48 (3) (1991) 153–178, <http://dx.doi.org/10.1007/BF00036629>.
- [67] M. Kassner, T. Hayes, Creep cavitation in metals, *Int. J. Plast.* 19 (10) (2003) 1715–1748, [http://dx.doi.org/10.1016/S0749-6419\(02\)00111-0](http://dx.doi.org/10.1016/S0749-6419(02)00111-0).
- [68] J. Bonneville, C. Coupeau, Quantitative atomic force microscopy analysis of slip traces in ni3al yield stress anomaly, *Mater. Sci. Eng. A* 483 (2008) 87–90.
- [69] J. Michel, C. Coupeau, Y. Nahas, M. Drouet, J. Bonneville, What can be learnt on the yield stress anomaly of Ni3Al using AFM observations, *Intermetallics* 50 (2014) 86–93, <http://dx.doi.org/10.1016/j.intermet.2014.02.013>.
- [70] V. Doquet, B. Barkia, Combined AFM, SEM and crystal plasticity analysis of grain boundary sliding in titanium at room temperature, *Mech. Mater.* 103 (2016) 18–27, <http://dx.doi.org/10.1016/j.mechmat.2016.09.001>.
- [71] B. Beucia, S. Queyreau, C. Kahloun, D. Chaubet, P. Franciosi, B. Bacroix, Plastic strain-induced grain boundary migration (SIBM) in pure aluminum: SEM in-situ and AFM examinations, *Int. J. Plast.* 115 (2019) 29–55, <http://dx.doi.org/10.1016/j.ijplas.2018.11.007>.
- [72] I. Šulák, K. Obrtlík, AFM, SEM and TEM study of damage mechanisms in cyclically strained mar-M247 at room temperature and high temperatures, *Theor. Appl. Fract. Mech.* 108 (2020) 102606, <http://dx.doi.org/10.1016/j.tafmec.2020.102606>.
- [73] S. Moore, R. Burrows, D. Kumar, M. Klouček, A. Warren, P. Flewitt, L. Picco, O. Payton, T. Martin, Observation of stress corrosion cracking using real-time in situ high-speed atomic force microscopy and correlative techniques, *npj Mater. Degradation* 5 (3) (2021) 1–10, <http://dx.doi.org/10.1038/s41529-020-00149-y>.
- [74] C. D'Hondt, V. Doquet, J.P. Couzinié, Direct monitoring of twinning/detwinning in a TWIP steel under reversed cyclic loading, *Mater. Sci. Eng. A* 814 (2021) <http://dx.doi.org/10.1016/j.msea.2021.141250>.